

AD-A267 728



200

Final Report for
SODIUM-MERCURY EXCIMER LASER, PHASE I

S DTIC
ELECTE
AUG 11 1993
A **D**

December 1992

prepared for

S.D.I.O.
TNI/SBIR, Pentagon, Room 1E167
Washington, DC 20301-7100

and

U.S. Army SDC
CSSD-AT-E
PO Box 1500
Huntsville, AL 35807-3801

as a result of Phase I contract
DASG-92-C-0141

This document has been approved
for public release and sale; its
distribution is unlimited.

by

PLEX Corporation
21 Addington Rd.
Brookline, MA 02146

93-18041



REPORT DOCUMENTATION PAGE

Form Approved
OMB No. 0704-0188

Public reporting burden for this collection of information is estimated to average 1 hour per response, including the time for reviewing instructions, searching existing data sources, gathering and maintaining the data needed, and completing and reviewing the collection of information. Send comments regarding this burden estimate or any other aspect of this collection of information, including suggestions for reducing this burden, to Washington Headquarters Services, Directorate for Information Operations and Reports, 1215 Jefferson Davis Highway, Suite 1204, Arlington, VA 22202-4302, and to the Office of Management and Budget, Paperwork Reduction Project (0704-0188), Washington, DC 20503.

1. AGENCY USE ONLY (Leave blank)	2. REPORT DATE DEC 1992	3. REPORT TYPE AND DATES COVERED FINAL REPORT JUN 1992 - DEC 1992	
4. TITLE AND SUBTITLE SODIUM-MERCURY EXCIMER LASER, PHASE 1		5. FUNDING NUMBERS CARN: 2C2367	
6. AUTHOR(S) Malcolm W. McGeoch		CONTRACT: DASG60-92-C-0140	
7. PERFORMING ORGANIZATION NAME(S) AND ADDRESS(ES) PLEX Corporation 21 Addington Rd. Brookline, MA 02146		8. PERFORMING ORGANIZATION REPORT NUMBER PLEX-003	
9. SPONSORING/MONITORING AGENCY NAME(S) AND ADDRESS(ES) Sponsored by: SDIO Innovative Science & Technology Office Managed by: US Army Strategic Defense Command PO Box 1500 Huntsville, AL 35807-3801		10. SPONSORING/MONITORING AGENCY REPORT NUMBER	
11. SUPPLEMENTARY NOTES			
12a. DISTRIBUTION/AVAILABILITY STATEMENT UNCLASSIFIED / UNLIMITED		12b. DISTRIBUTION CODE	
13. ABSTRACT (Maximum 200 words) This Phase 1 work addresses the technology required to test the sodium-mercury excimer laser concept. Calculations of the optimum laser excitation conditions show that a gain of 2.8% /cm should be achievable in the 1.2 micron region for a specific discharge power input of 20kW/cm ³ . At the lower power input of 2kW/cm ³ the projected gain is 1.5%/cm. The calculations consider the electron energy distribution function and collisional dissociation of NaHg(A) state molecules. Ultraviolet pre-ionisation was shown to be a viable route to the attainment of high power discharges in this system. An experimental test of 600oC cell technology was performed, in which windows, leadthroughs and a close-out valve were cycled repeatedly to that temperature.			
14. SUBJECT TERMS Laser, Excimer, Sodium, Mercury, Cell, Technology, Gain, Calculations.		15. NUMBER OF PAGES 40	
		16. PRICE CODE	
17. SECURITY CLASSIFICATION OF REPORT UNCLASSIFIED	18. SECURITY CLASSIFICATION OF THIS PAGE UNCLASSIFIED	19. SECURITY CLASSIFICATION OF ABSTRACT UNCLASSIFIED	20. LIMITATION OF ABSTRACT UL

CONTENTS

Section	Page Number
1.0 Abstract of Phase I Results	2
2.0 Illustration of Phase I Results	3
3.0 Phase I Experimental Results (Proof of Test Cell)	4
4.0 Phase I Theoretical Results	9
4.1 NaHg: The A-X Transitions	9
4.2 Boltzmann Calculation of Electron Energy Distribution function	14
4.3 Kinetic Model of Gain Experiment and Laser	20
4.3.1 3-body complexing and dissociation	23
4.3.2 Spontaneous and stimulated emission	24
4.3.3 Inelastic and superelastic electron rates	27
4.3.4 Gain projections from model	27
4.3.5 Oscillation projections from model	29
4.4 Preionisation/Initiation of NaHg Discharge	32
4.4.1 Avalanche requirements for NaHg	32
4.4.2 Ultraviolet preionisation	33
4.4.3 Final stage preionisation by energy transfer	35
5.0 Hazard Assessment and Preliminary Hazard List	39
6.0 References	40

DTIC QUALITY INSPECTED 3

Accession For	
NTIS CRA&I	<input checked="" type="checkbox"/>
DTIC TAB	<input type="checkbox"/>
Unannounced	<input type="checkbox"/>
Justification	
By	
Distribution /	
Availability Codes	
Dist	Availability for specification
A-1	

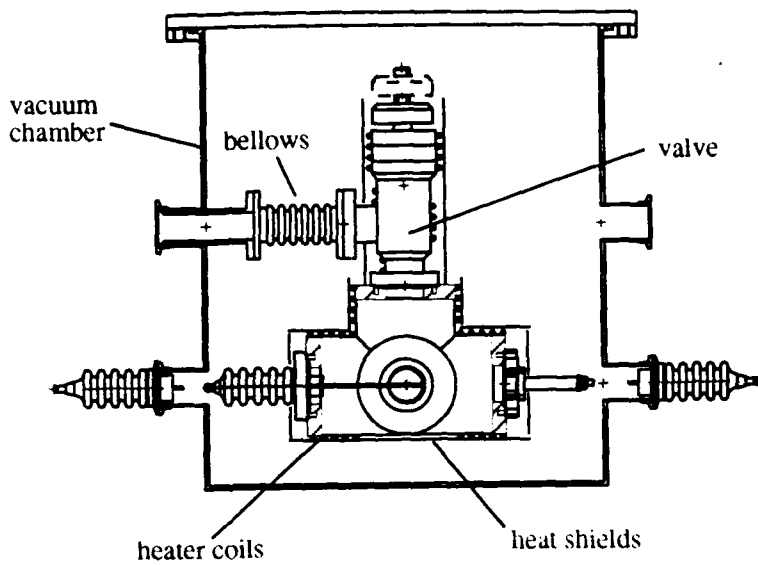
1.0 The Sodium-Mercury Laser . Abstract of Phase I Results

A new laser of exceptionally high efficiency (30%) appears to be possible, based on discharge excitation of the sodium-mercury excimer NaHg(A) state. The most likely waveband for oscillation is 1.0 - 1.3 μ m, but it is possible that the transition will be tunable over a wider range. This project sets out to determine the lasing performance and scalability of NaHg and to develop a pre-commercial version of the laser at a power level (1.5kW) appropriate for many industrial welding, cutting and heat-treating uses.

The reason that this promising system has not been much explored to date is that a moderate temperature (580 - 600°C) is required to obtain sufficient sodium vapor pressure for efficient laser excitation. Because conventional bakeable vacuum equipment is only rated to 450°C, previous work on the NaHg system has used vessels of sapphire or alumina, bonded by high temperature ceramic frits and brazed to niobium and then to stainless steel in order to carry a close-out valve. As a prerequisite for any fieldable device and indeed for the proposed laser test experiments a rugged metal cell had to be devised, with laser quality sapphire windows.

In Phase I we have succeeded in designing and testing a metal cell apparatus which has been cycled repeatedly to 600°C and can contain a 20cm discharge. The cell contains three categories of component:- sapphire windows, current leadthroughs and a close-out valve. The conventional kovar-sapphire/alumina seal can be used because there is a good thermal expansion match up to 650°C, however a higher temperature braze is used, and two further steps are taken. The whole cell is placed in a vacuum to prevent oxidation, and nickel replaces copper as the gasket material, for improved compatibility with the metal vapor and reduced oxidation. A combination of ceramic-insulated, nichrome wire heater elements and nickel heat shields was used to bring the test cell to temperature with relatively low radiative and conductive heat losses. In conclusion, a usable apparatus has been demonstrated for the lasing tests proposed in Phase II of the project.

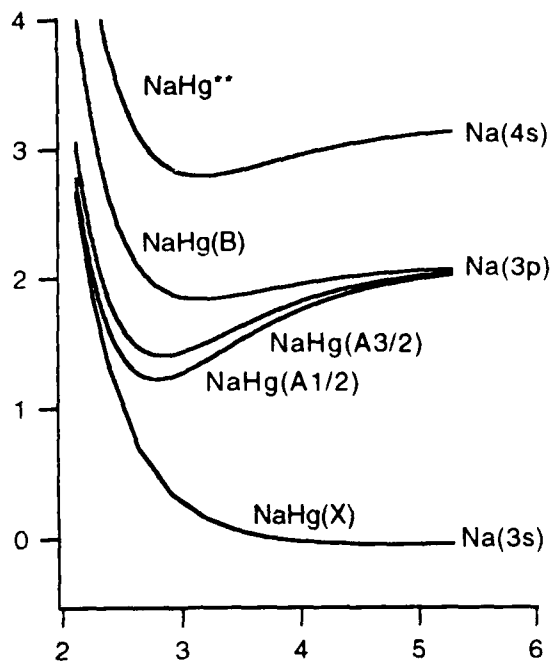
A number of theoretical calculations were performed in order to specify the optimum lasing test conditions, and determine the method of pre-ionisation necessary for the creation of a uniform volume discharge. It was found that ultraviolet (uv) preionisation was particularly efficient in this system, and that an energy transfer from Hg to Na helped to accelerate the growth of ionisation once a certain level (10^{11} electrons per cm^3) had been reached by uv preionisation. Optimum laser gain (2.8% cm^{-1}) is predicted for a specific discharge power of 20kW cm^{-3} , although a gain as high as 1.5% cm^{-1} is predicted at excitation power as low as 2kW cm^{-3} . Typical lasing operation was simulated, showing that the buildup time was 0.2 μ sec, and that following a "gain-switched spike" the steady laser efficiency was expected to be 30%. The test cell built in Phase I is designed to reach the 2 - 20kW cm^{-3} regime relevant to a Phase II test of NaHg laser efficiency.



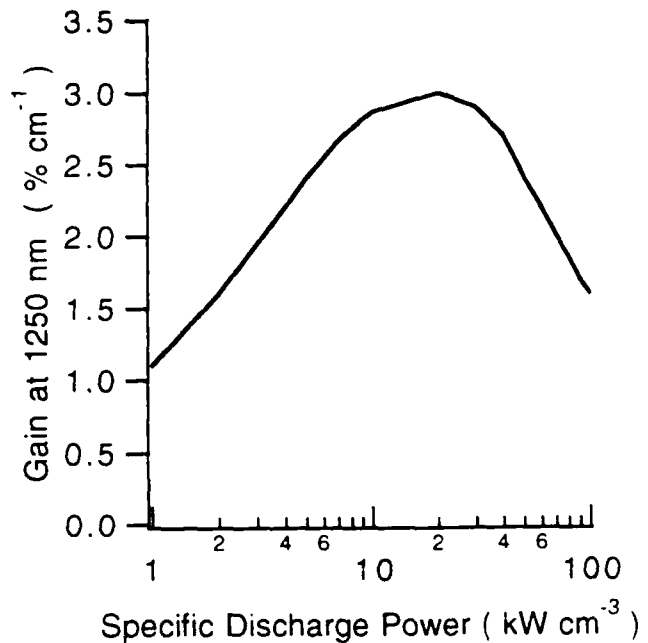
(a) Drawing of 20cm discharge test cell in vacuum tank.



(b) View of test cell after three cycles to 600°C



(c) Molecular potentials of principal sodium mercury excimer states



(d) Calculated sodium mercury laser gain vs discharge power.

FIG. 1-1 Illustration for Abstract of Phase I Results.

PLEX Corporation, Brookline MA. Research Sponsored by SDIO/IST and managed by the U.S. Army Strategic Defense Command, Huntsville, Alabama. Contract DASG 60-92-C-0141.

3.0

Phase 1 Experimental Results

The most important Phase 1 experimental objective, to establish a hot cell technology suitable for Na/Hg laser experiments, has been achieved. In the laser modeling we found that a Na density of 2×10^{17} atoms cm^{-3} is required in order to provide useful gain. This requires a temperature of 580°C in a pellet of pure Na situated in the coolest part of the cell, and hence the cell components in general have to be able to withstand 600°C , approximately. These components consist of

- a) a close-off valve,
- b) sapphire windows,
- c) high voltage leadthroughs.

The cell itself can be made of 304 stainless steel, which is compatible with Hg/Na vapors at these temperatures.

When the study began it was known that over a temperature range up to 1000°C there was a very good thermal expansion match between sapphire or alumina ceramic (the window and insulator materials) and niobium. In fact this combination is used in high temperature sodium-mercury street lamps. However the use of niobium carries the penalty that it is very readily oxidised in air at temperatures as low as 200°C . For this reason street lamps have an evacuated glass envelope around the central arc tube. Shortly after the beginning of Phase 1 it was realised that the thermal expansions of nickel-iron 'Kovar' and sapphire (alumina) were excellently matched up to 650°C (Figure 3-1). In fact, the combination is used in many commercially-available vacuum windows and HV leadthroughs. However all of these components are only rated for bake-out at 450°C maximum. Discussion with the principal manufacturer of these components, ISI Inc., revealed that there were two reasons for this limit:

1. The braze material commonly used (Ag-Cu) begins to soften at 700°C .
2. Bake-out is usually in air and the copper gaskets used in the vacuum seal oxidise rapidly in air at 650°C . Even Ni-plated gaskets oxidise in time.

However ISI suggested the use of Ticusil 5 braze alloy which was good to 800°C and it was decided to employ a vacuum region around the test cell, not only to prevent oxidation of the Ni gaskets but also to provide thermal insulation; a safety zone for metal containment in the event of a window or leadthrough breakage; and to prevent oxidation of the nichrome heater wires which would operate at up to $1,000^\circ\text{C}$, locally. Special sapphire windows of 1" clear diameter and two designs of HV leadthrough were all obtained from ISI with the manufacturer's expectation (but not guarantee) that service would be good up to 650°C in vacuum.

The design of the test cell is shown in Figure 3-2. Internal to the cell we arranged for a $1\text{cm} \times 1.5\text{cm} \times 20\text{cm}$ discharge volume between two electrodes. One of the electrodes was supported on a 30kV ceramic leadthrough, and the other electrode, while grounded, had an internal pre-ionisation circuit supplied by a 20kV ceramic leadthrough. At each end of the cell was a sapphire window. These windows are cut from single crystal uv grade sapphire (which also has the best IR

Differential Thermal Expansion of Seal Components

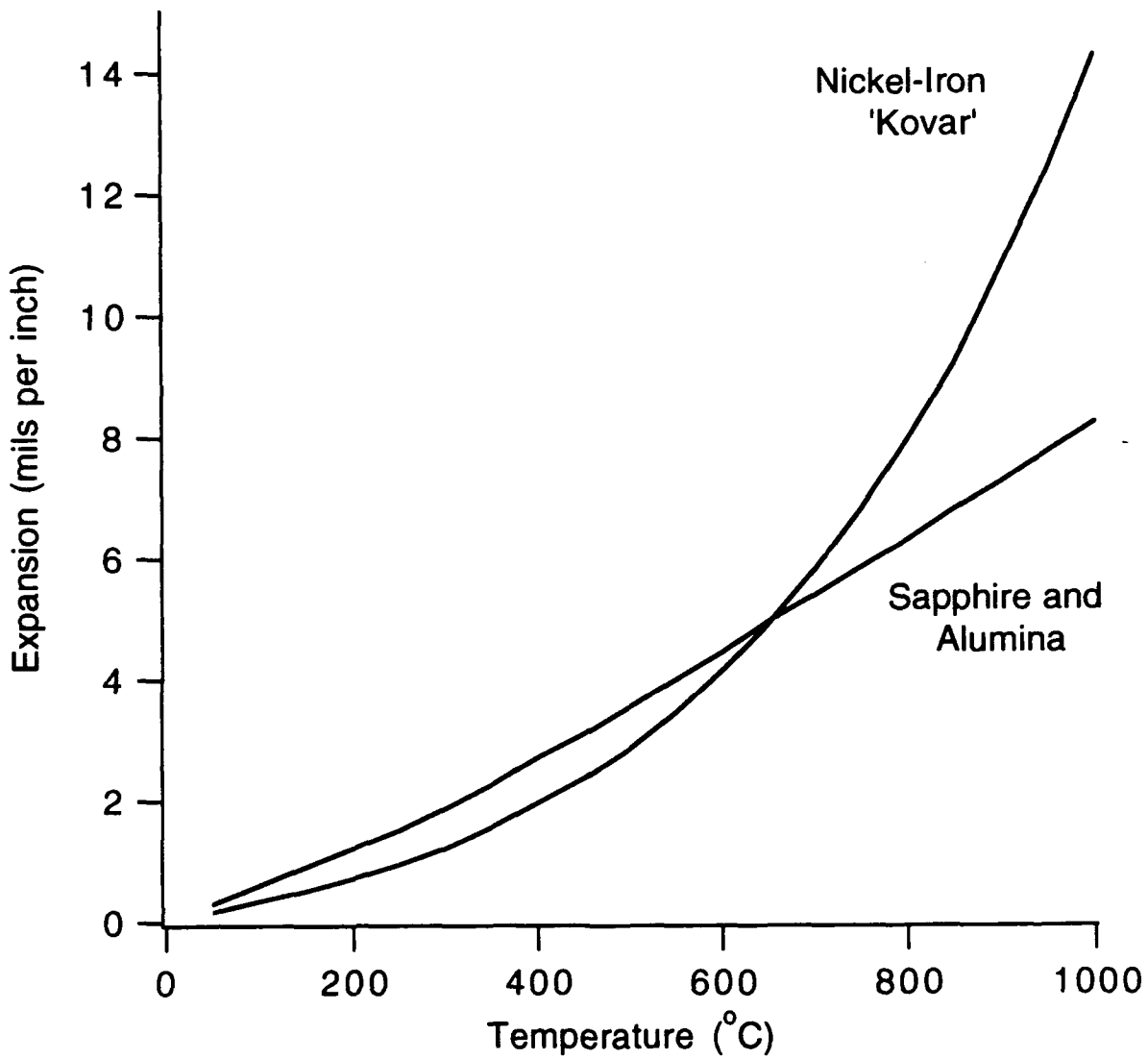


FIG. 3-1 Differential thermal expansion of kovar and sapphire/alumina seal materials. This combination functions up to 650°C.

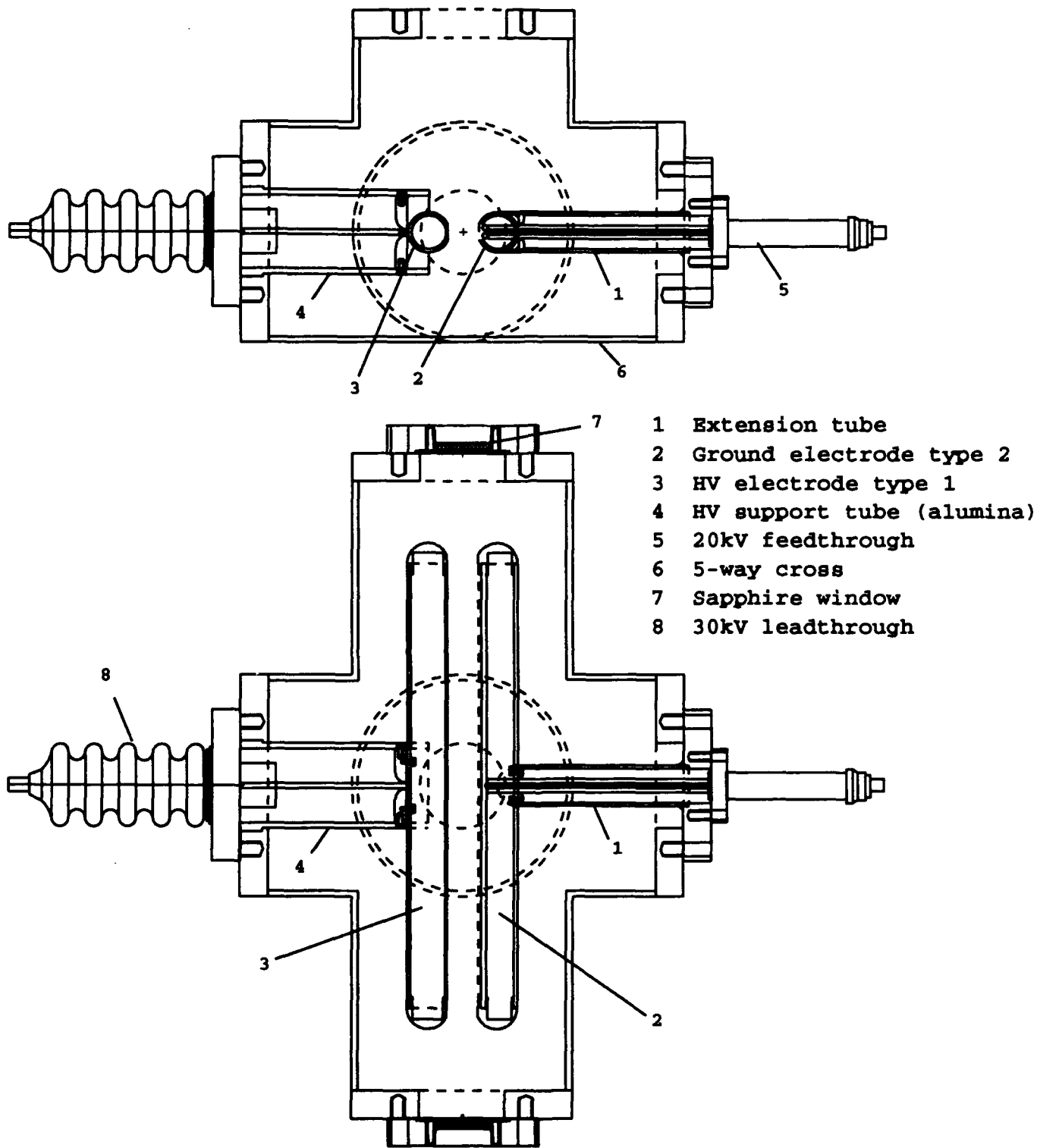


FIG. 3-2 Electrode design of 20cm discharge test cell

transmission) and optically polished. They appear to be of laser quality. Before attempts at lasing, however, an interferogram will be taken on each window.

The 20cm test cell is mounted inside a 16 inch diameter x 18 inch tall 10^{-4} torr vacuum chamber (Fig. 3-3) which has heater and thermocouple leadthroughs. The test cell itself sits on ceramic stands and is surrounded by a heat shield of 0.010 inch nickel sheet. Nickel was chosen because of its low emissivity (0.1) and its rigidity up to 700°C . Heat is provided to the cell via four windings of 0.025" nichrome wire each of resistance 15 ohms which are insulated with flexible woven ceramic sleeve (Nextel 312) rated at 1200°C and compatible with vacuum. The windings are powered by individually adjusted SCR controllers slaved to a master thermocouple. The temperature is recorded at five locations on the cell (window, HV leadthrough, valve and at each end of the steel bellows section, which serves as a thermal break. The valve (MV150 from Huntington) was nominally rated at 450°C but again the limitation is oxidation in air, and we have shown that it is capable of operation in vacuum up to 600°C .

The cell was heated 3 times to 600°C and its cooling curve recorded in order to estimate the balance of heat loss between conduction and radiation. The rate of heat loss at 600°C was 470W, comprising 280W due to radiation and 190W due to conduction. The relatively low radiation loss is attributed to the low emissivity of the nickel heat shield, estimated to be 0.15 from the data. After each heating cycle the vacuum integrity of the test cell was confirmed by letting air into the outer chamber while maintaining the cell under vacuum.

Metal vapor was not employed in these tests because the compatibility of Na and Hg with the cell materials is assured by previous work. The most important point is that sapphire remains optically clear in contact with this mixture at 600°C , as seen in previous tests.

In conclusion, the Phase I experiments have demonstrated a viable technology for the accomplishment of the proposed laser experiments of Phase II. More than this, the Phase I test cell is fitted with 20cm electrodes so that it is immediately usable for the first discharge tests of Phase II. Possibly the 20cm discharge will also be usable for the first oscillation experiments.

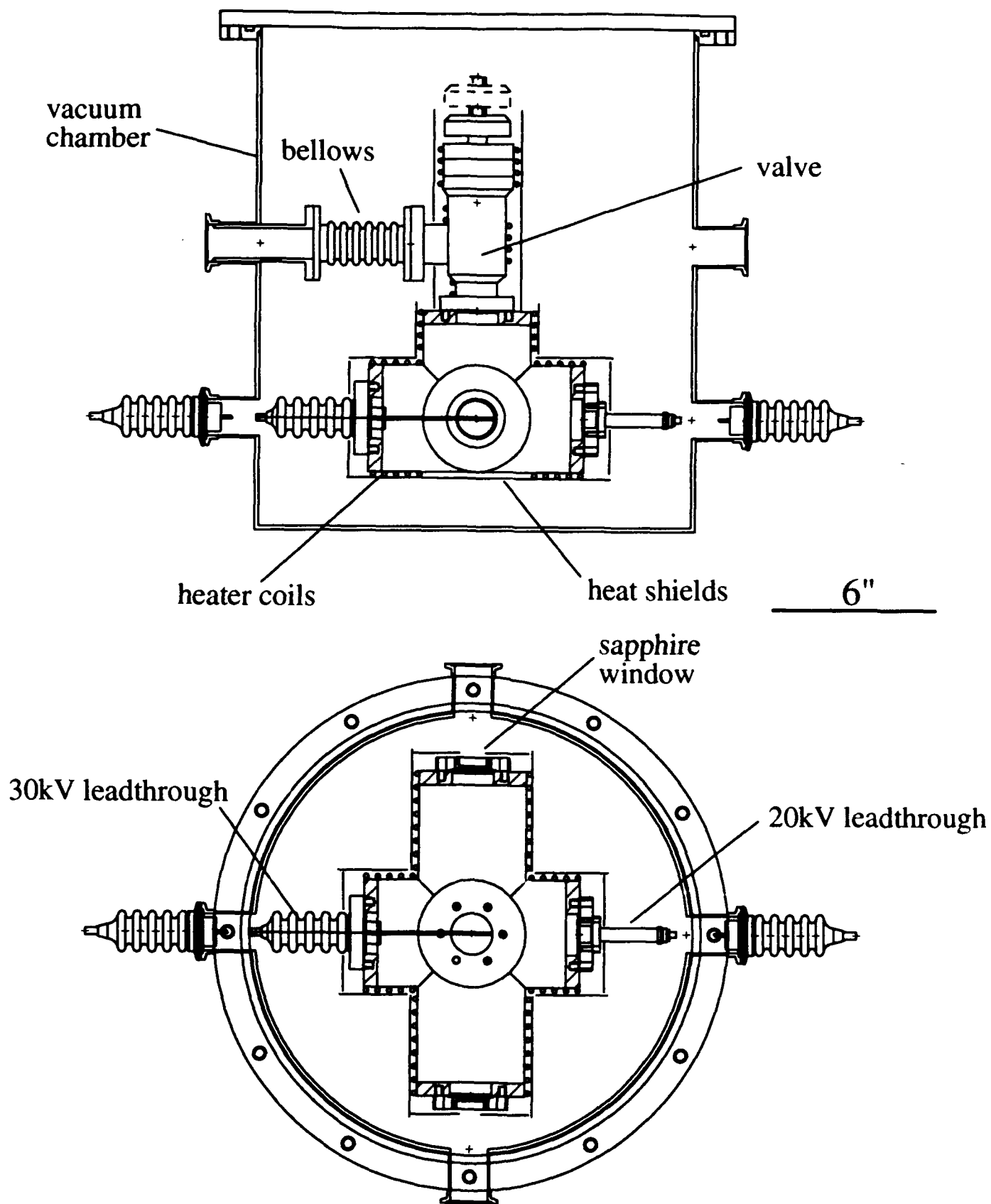


FIG. 3-3 Test cell mounted inside vacuum chamber

4.0

Phase I Theoretical Results

4.1 NaHg: The A - X Transitions

Although the NaHg(A) state has been described as a single state in all prior work, including the PLEX SBIR proposal, it is in fact composed of two components, A(1/2) and A(3/2), which have recently been estimated [1] to lie 0.18eV apart, with the A3/2 at higher energy than the A1/2 (Figure 4-1). In this section we re-visit the calculation which relates the shapes of the A and X potentials to the fluorescence (or gain) profiles and show that a set of potential parameters can be chosen that includes state splitting and yet is compatible with previous measurements.

Prior experiments gave the following parameters for an assumed single A state:

1. Huwel et.al. [2] scattered Na(3p) atoms off ground state Hg atoms to obtain $D_e = 0.755\text{eV}$ for the binding energy, and $r_e = 3.46 \text{ \AA}$ for the equilibrium internuclear distance.
2. Schlejen and Woerdman [3] measured absorption in the red wing of the Na(3p - 3s) transition to obtain $D_e = 0.755\text{eV}$ and $r_e = 3.1 \text{ \AA}$.
3. McGeoch (unpublished) fitted fluorescence data to obtain the approximate values $D_e = 0.77\text{eV}$ and $r_e = 3.03 \text{ \AA}$.

The theoretical curves of reference [1] were least squares fitted by Morse potentials, in order to use them in an easily available form in the fluorescence calculation. The fit was constrained to have the correct asymptotic energy corresponding to the Na3p state. This corrected the excess binding of about 0.1eV expected in the theory [1]. The Morse potential is of the form:

$$V(r) = D_e \left[1 - e^{-\beta(r-r_e)} \right]^2 - D_e$$

The fitted Morse potentials are shown in Figure 4-1, and have parameters

A1/2	$D_e = 0.88\text{eV}$	$r_e = 2.80\text{\AA}$	$\beta = 1.24$
A3/2	$D_e = 0.70\text{eV}$	$r_e = 2.85\text{\AA}$	$\beta = 1.27$

It was found that these r_e values, which are lower than previous experimental estimates, did not match the experimental fluorescence curve (Figure 4-2). The set of Morse parameters finally chosen was:

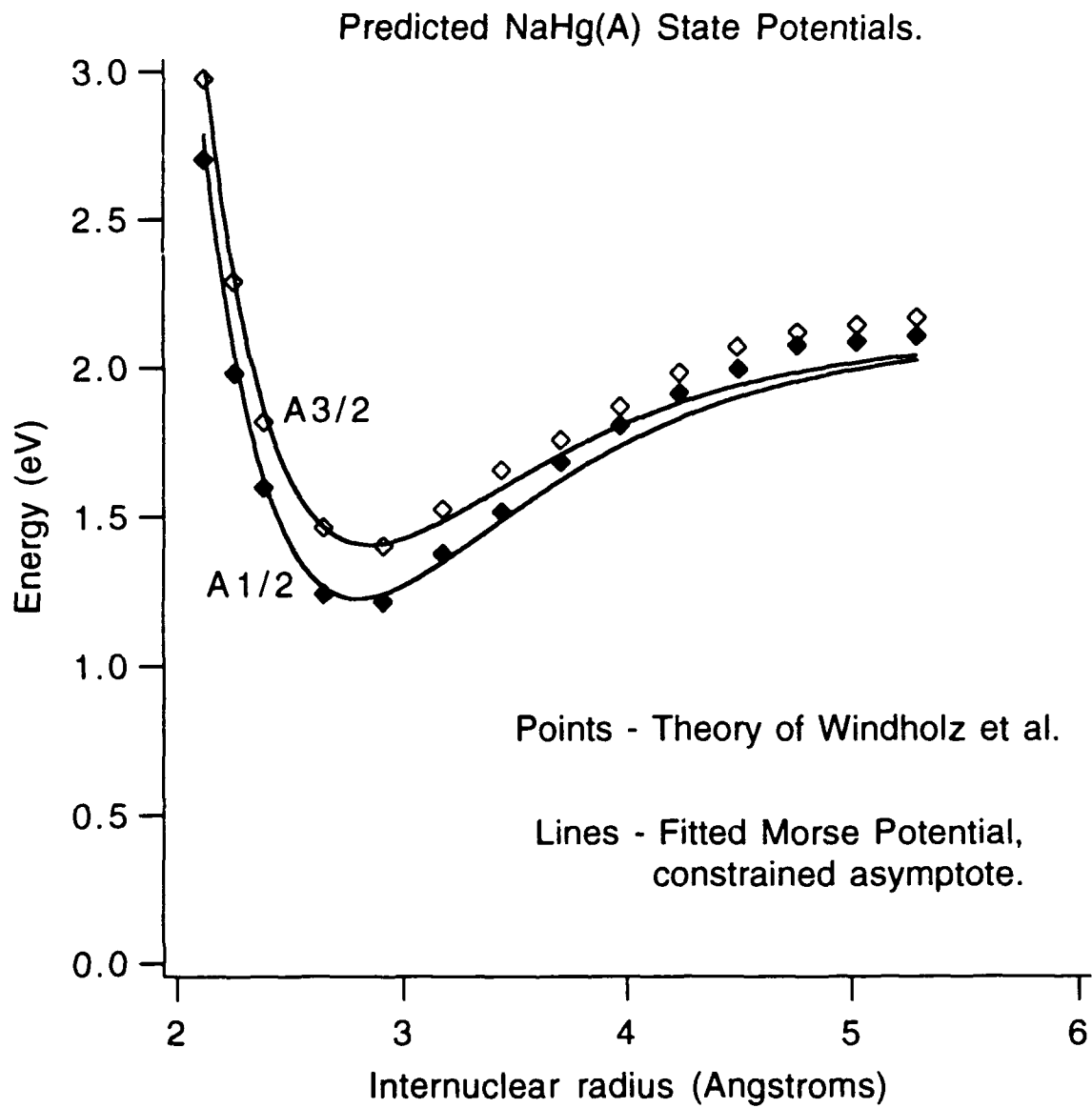


FIG. 4-1 Theoretical NaHg(A) state potentials [1] and fitted Morse potentials with asymptotes constrained to match Na3p energy.

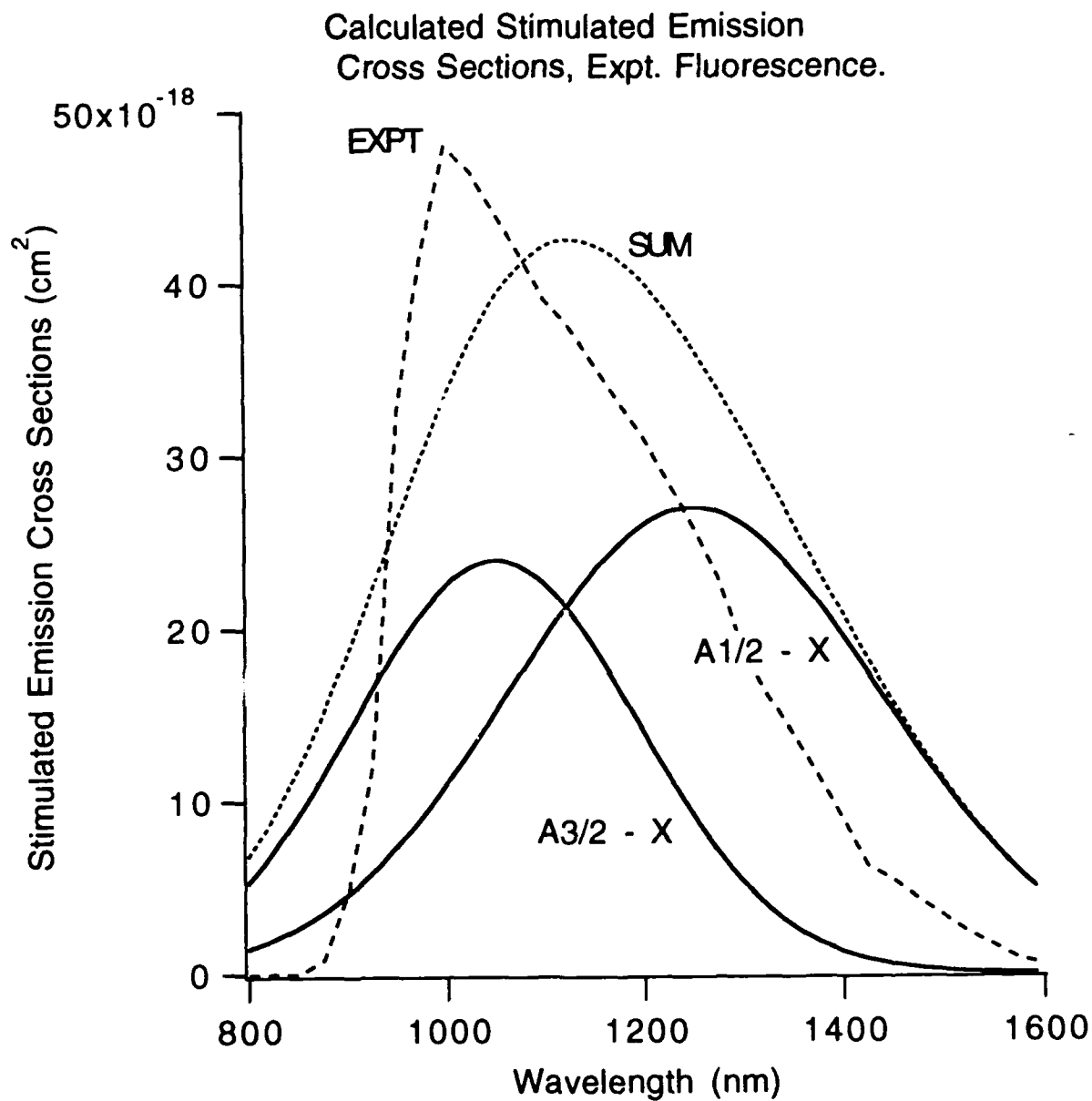


FIG. 4-2 Stimulated emission cross sections for NaHg(A-X) transitions (solid curves). Arithmetic sum of cross sections shown as dotted curve (not weighted by relative state populations) and experimental fluorescence curve from prior work shown as dashed curve. The experimental detector calibration was uncertain below 900nm.

A1/2	$D_e = 0.88\text{eV}$	$r_e = 3.10\text{\AA}$	$\beta = 1.24$
A3/2	$D_e = 0.70\text{eV}$	$r_e = 3.10\text{\AA}$	$\beta = 1.27$

The gain profiles were calculated using the classical form of York et al. [4]. Any one frequency ν in the A-X fluorescence spectrum is generated at an internuclear distance R_C representing a Condon point for that frequency. The emitted frequency is related to the A and X potentials by

$$h\nu(R_C) = V_A(R_C) - V_X(R_C) + h\nu_0$$

where $h\nu_0$ is the frequency of the Na(3p - 3s) transition. The NaHg(X) potential has been determined experimentally by Huwel et al. [5].

The total contribution to spontaneous emission at frequency ν is the sum of all Condon point contributions, weighted by the thermal distribution in the upper state and the volume of R space per unit frequency interval. Therefore

$$S(\nu) \propto \sum_{R_c} \frac{4\pi R_c^2 A(R_c)}{\left. \frac{d\nu}{dR} \right|_{R_c}} \exp\left(\frac{-V_A(R_c)}{kT}\right)$$

The units of $S(\nu)$ are photons per unit time per unit frequency interval. In this expression $A(R_C)$ is the spontaneous emission rate at $R = R_C$. $A(R_C)$ is proportional to the oscillator strength $f(R)$ which is projected by Windholtz et al. [1] to decrease with internuclear separation, and the stimulated emission (gain) cross section is proportional to $\lambda^2 S(\nu)$. Using their oscillator strength, parametrised as

$$f_{A-X} = -0.1552 + 0.068R + 0.003336R^2$$

with R in Angstroms, the gain cross sections were calculated for the A1/2 - X and A3/2 - X transitions (Figure 4-2). The above set of potentials gives maximum gain wavelengths of 1250nm and 1050nm, respectively. The sum of the two gain cross section curves is also shown, to illustrate (not to scale) the relative gain profile that would result from equal populations in each state. The experimental fluorescence, also shown (scaled) on Figure 4-2, peaks at 1000nm and is a sum of contributions from the two emission bands. The experimental fluorescence could not be recorded accurately below 900nm because of a detector cut-off. There is not sufficient fluorescence data to say whether in that experiment the two states had reached thermal equilibrium or not.

Assuming that both A states form with the same efficiency, and relaxation is slow compared to radiation ($\tau_{\text{RAD}} \sim 200\text{nsec}$), the anticipated gain spectrum will then be the sum of the two gain curves. However it is likely that partial relaxation

occurred in the fluorescence experiment, and even more likely that substantial relaxation from 3/2 to 1/2 will occur in the higher density laser conditions. The gain optimum is therefore expected to be closer to 1250nm. In section 4.3 the kinetic model includes relaxation in calculations of the gain and laser performance in typical discharge conditions.

There is a small absorption at the laser wavelength due to the inverse of the gain process, free-bound absorption from colliding pairs of ground state sodium and mercury atoms. The absorption coefficient is given by

$$K(\nu) = \frac{\lambda^2 g_X [Na][Hg]}{8\pi g_A} \sum_{R_c} \frac{4\pi R_c^2 A(R_c)}{\left. \frac{d\nu}{dR} \right|_{R_c}} \exp\left(\frac{-V_X(R_c)}{kT}\right)$$

where g_X and g_A are the state degeneracies. For typical laser conditions of $T = 1000\text{K}$ $[Na] = 2 \times 10^{17} \text{cm}^{-3}$ $[Hg] = 2 \times 10^{19} \text{cm}^{-3}$ this absorption is $0.1\% \text{ cm}^{-1}$ (at 1250nm), very much less than the typical gain of approx. $2\% \text{ cm}^{-1}$.

4.2 Boltzmann Calculation of Electron Energy Distribution Function.

A set of the most important low-lying atomic energy levels (Figure 4-3) was used in a calculation of the electron energy distribution function. The energies of some of the more important molecular species are also shown for comparison. The calculation employed the Hg excitation cross sections of Rockwood [6], and the Na cross sections of Schlie [7] and of Shuker et al. [8]. Some results for 1% Na, 99% Hg that are used in the following sections are given in Figures 4-4, 4-5, 4-6 and 4-7.

The drift velocity is shown in Figure 4-4. Figure 4-5 shows that the fraction of discharge power going into the excitation of Na(3p), the laser precursor level, is 70% at $E/N = 5 \times 10^{-17} \text{ V cm}^2$ and rises to over 90% at $E/N = 1 \times 10^{-16} \text{ V cm}^2$, for 1% sodium in the mix. Anywhere in this range the laser will be highly efficient, as modeled in the following section, but the ionisation rate, in conjunction with the external circuit, determines the operating E/N that will exist, and once the discharge current reaches several A cm^{-2} , the multiple step ionisation of sodium exceeds recombination for E/N greater than $5 \times 10^{-17} \text{ V cm}^2$, ensuring that this lower value will be experienced in operation. Higher than 70% fractional power into Na(3p) could be achieved at this E/N by increasing the sodium fraction above 1%. For example, at 2% Na the fractional power would rise to 85% at this E/N . However, the cost of working at higher Na fraction is less safety margin on the braze technology of the laser cell. The cell temperature would have to rise by approx. 50 °C just to double the Na density in the range of interest (around $2 \times 10^{17} \text{ cm}^{-3}$). At $2 \times 10^{17} \text{ cm}^{-3}$ the cell temperature is 580°C.

Although calculations show that the discharge will be self-sustaining at $E/N = 5 \times 10^{-17} \text{ V cm}^2$, the discharge will not ignite at this E/N , because the ionisation mechanism at low electron density is either via Hg(3P_1) or Na^+ excitation, requiring E/N in excess of $1.5 \times 10^{-16} \text{ V cm}^2$ (Figure 4-6). The use of preionisation to assist this process is the subject of Section 4.4.

Finally, the excitation rates for the Na(3p) and Na(4s) levels are given in Figure 4-7. Because the superelastic rates (for the reverse processes) are very high it is necessary to consider them also as the discharge power is increased. They contribute to the slow decline in predicted laser efficiency at discharge powers in excess of 10 kW cm^{-3} (following section).

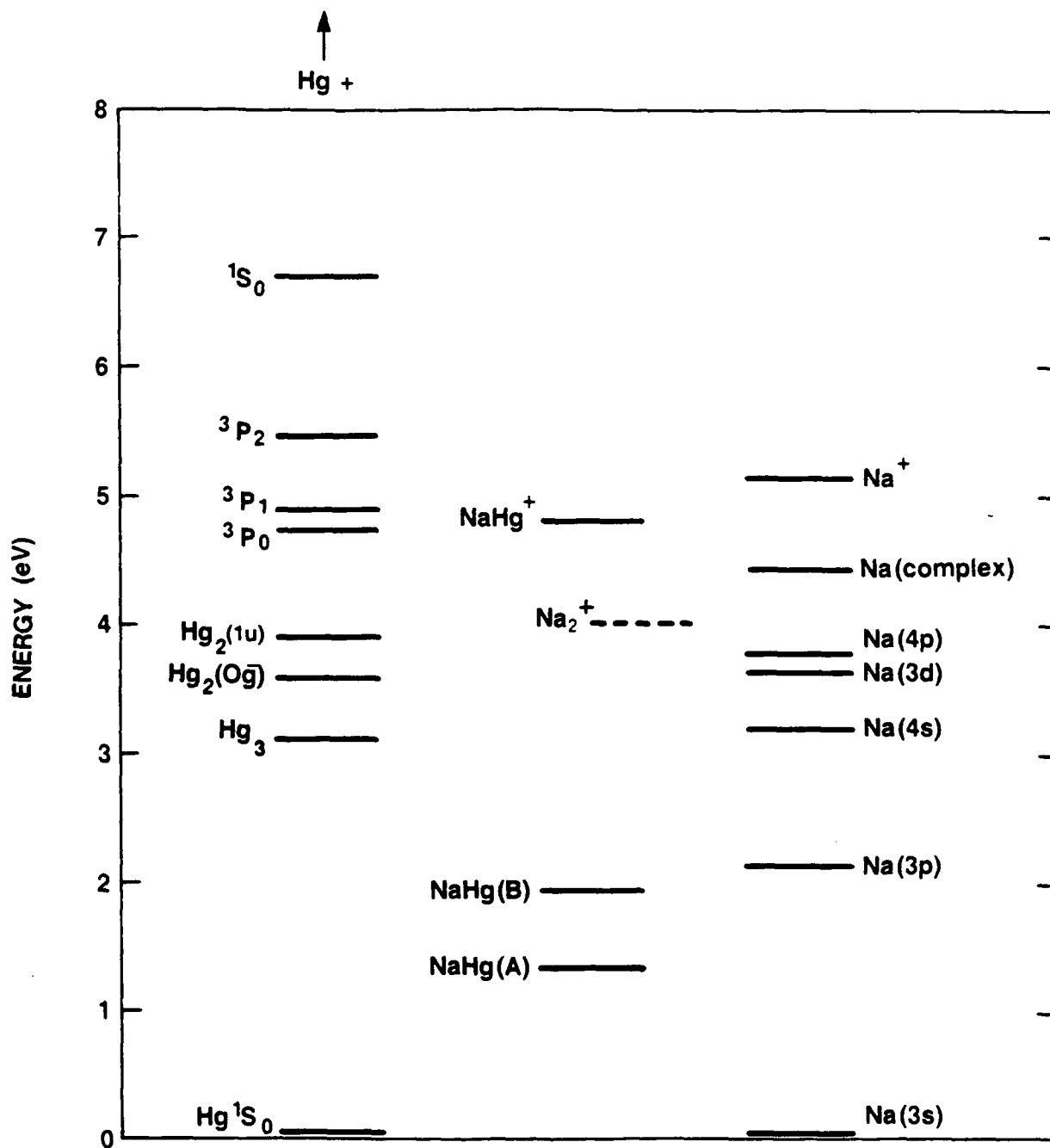


FIG. 4-3 Set of the more important atomic and molecular energy levels for the NaHg system. Seven atomic Na levels and seven atomic Hg levels (five shown) were used in the Boltzmann calculation.

DRIFT VELOCITY vs E/N for 1 % Na, 99% Hg

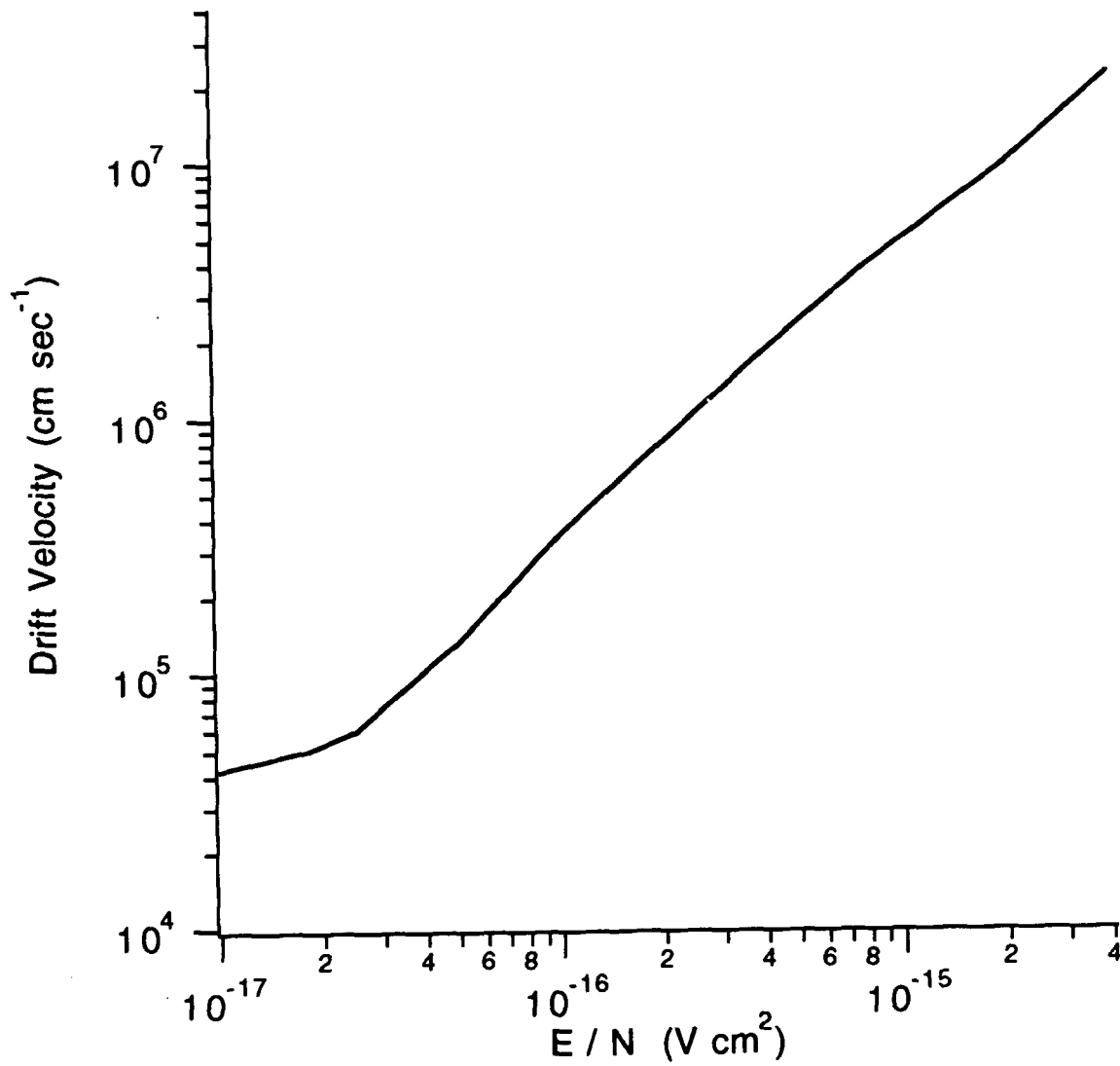


FIG. 4-4 Electron drift velocity calculated for a 99% Hg, 1% Na mixture.

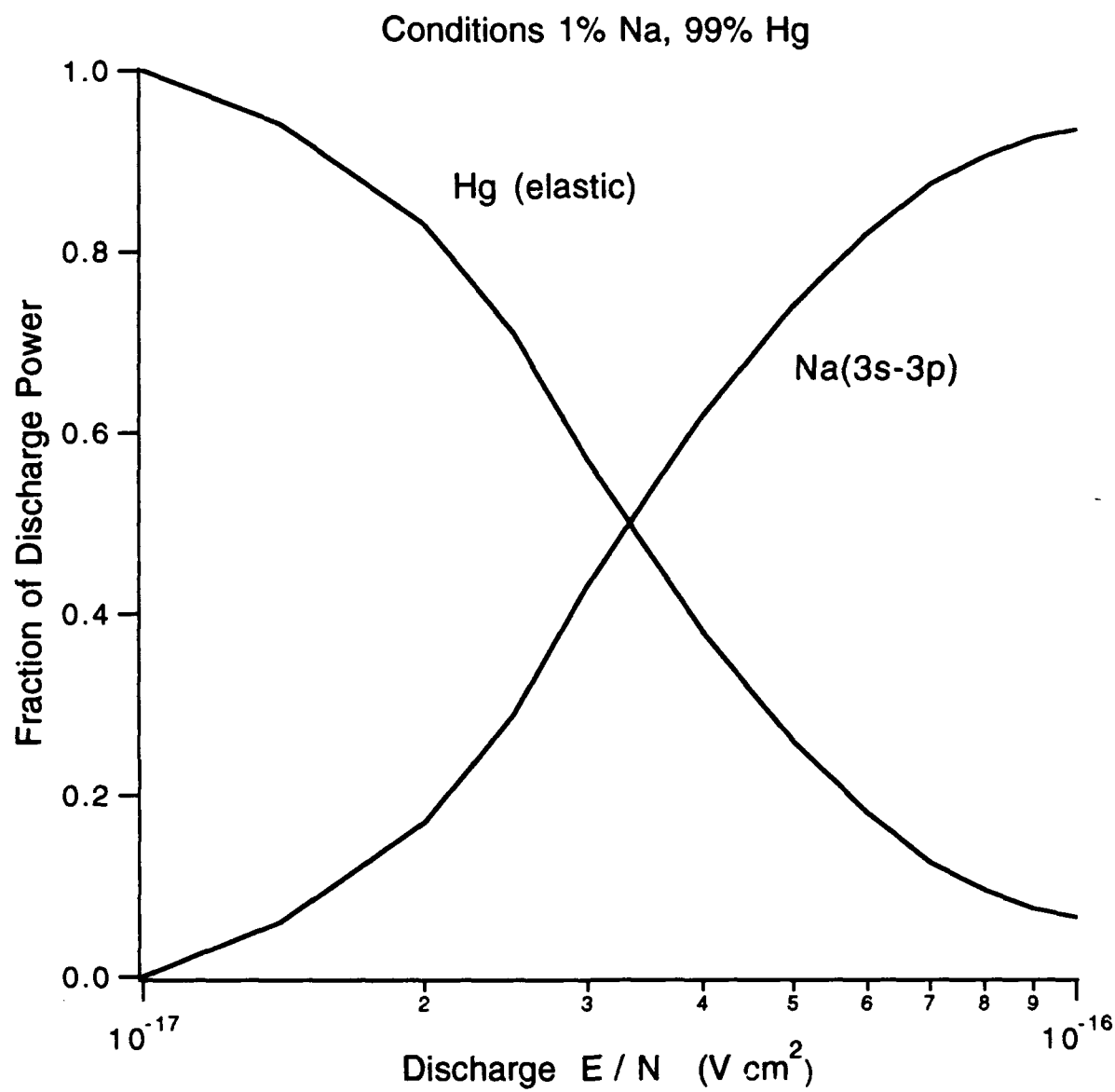


FIG. 4-5 Fraction of discharge power going into Na(3p) excitation and Hg elastic losses as a function of E/N for a 1%Na, 99%Hg mixture.

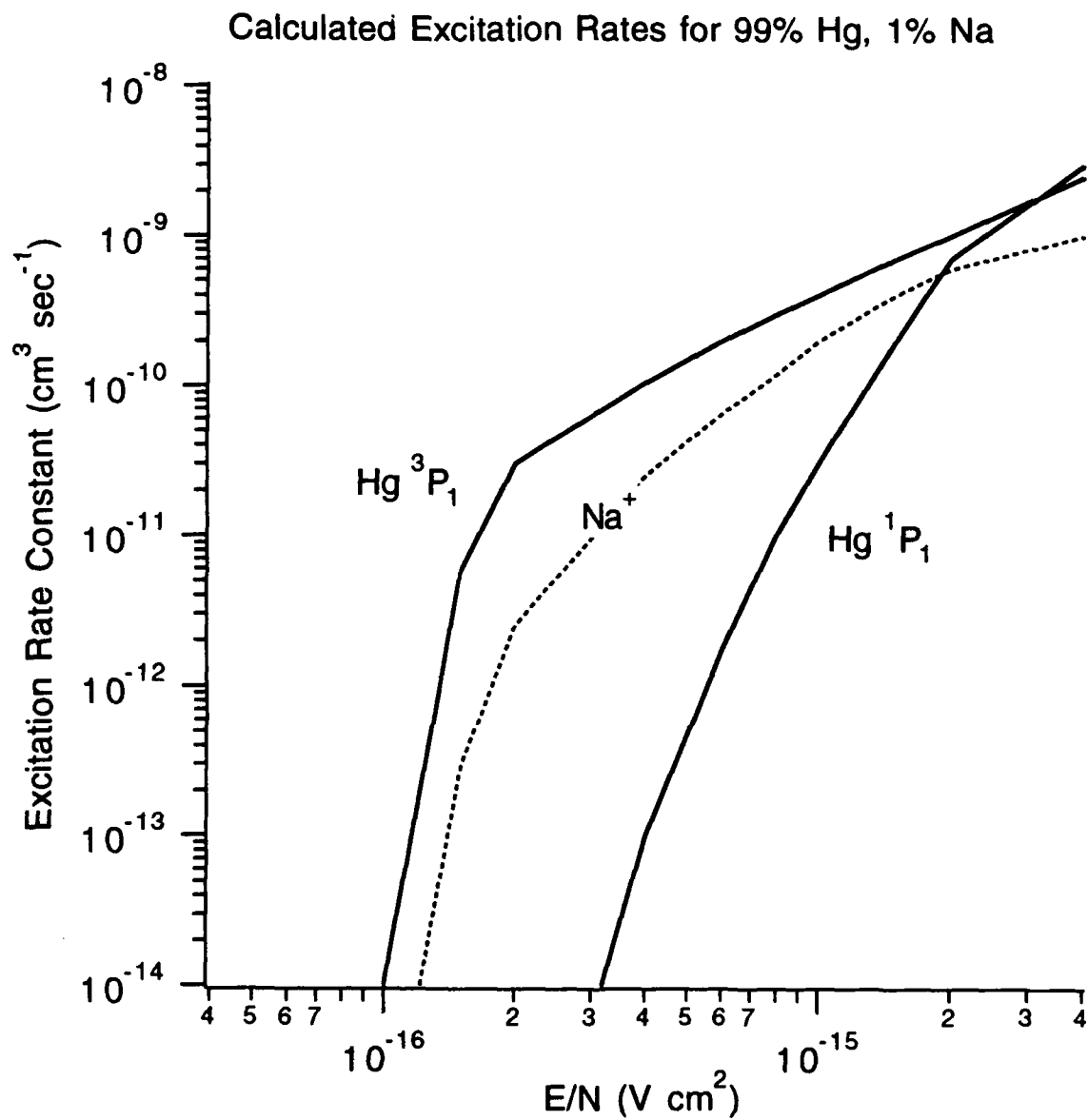


FIG. 4-6 Rate constants for mercury atomic excitation and sodium ionisation as a function of E/N at low electron density.

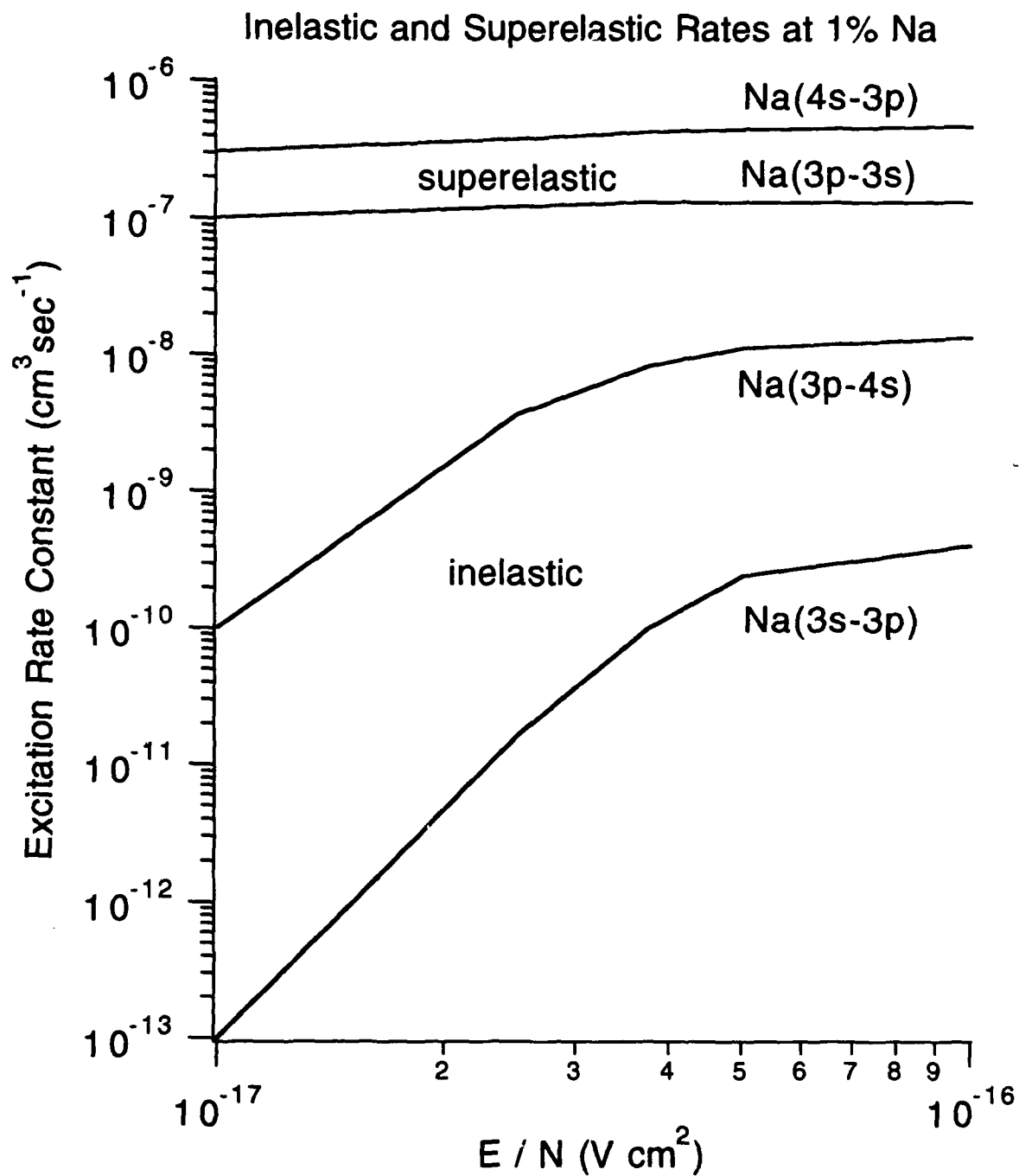


FIG. 4-7 Inelastic and superelastic rates between Na3s, 3p and 4s states at high electron density ($\sim 5 \times 10^{14} \text{cm}^{-3}$) in 1%Na, 99%Hg mixture.

4.3

Kinetic Model of Gain Experiment and Laser

In this section we estimate the gain that would be expected in a sodium-mercury discharge as a function of the discharge power per unit volume that is applied. The results show that a specific power of $1 - 2 \times 10^4 \text{ Wcm}^{-3}$ gives the highest gain, and is therefore optimum for our gain experiment. We also simulate the lasing performance and find that a laser efficiency of 30% should be obtained at specific powers up to 3kW cm^{-3} , decreasing to 25% at 10kW cm^{-3} . If these projections are correct an optimally efficient laser would be designed to operate in the pulsed mode at up to 3kW cm^{-3} . The energy deposition (established in previous metal vapor discharges) would be 30J per litre, implying a pulse duration of 10 μ sec. At 30% efficiency the extracted specific energy per pulse would be 9J per litre.

The three low-lying NaHg states A(1/2), A(3/2) and B, previously discussed, will dominate the behaviour of the model, but a higher NaHg state will also form, designated NaHg**, representing principally the behaviour of the NaHg(C,D) species [1] asymptotic to the Na(4s) state which forms in the discharge.

An overall view of the states involved in the kinetic model is given in Figure 4-8.

The rates for excitation and de-excitation of Na(3p) and Na(4s) (via Na(3p)) by electron collisions are obtained by running the Boltzmann solver (previous section) for a specified discharge E / N . These four numbers are inserted into the kinetic code as constant driving terms. Direct excitation to Na(4s) from the ground state Na(3s) is forbidden. In addition to the above electron collisional rates, we consider molecule formation via 3-body complexing and the reverse process, collisional dissociation. Electron induced mixing of the laser upper levels could also be important, and electron collisional destruction of these levels is included. It is considered that collisional de-excitation by Hg should be rapid from the B state to the A states, because of the curve crossings at large internuclear distance. Finally, in addition to spontaneous and stimulated emission, the possibility of NaHg₂ trimer formation is considered, merely as a worst case scenario, although there is no experimental evidence for trimer formation. Metal vapor trimers exist in the group IIB mixed metal systems but there may not be so much binding in the NaHg system. All the above processes are listed in Table 1. A more detailed discussion of some of the rates will be given in the following paragraphs.

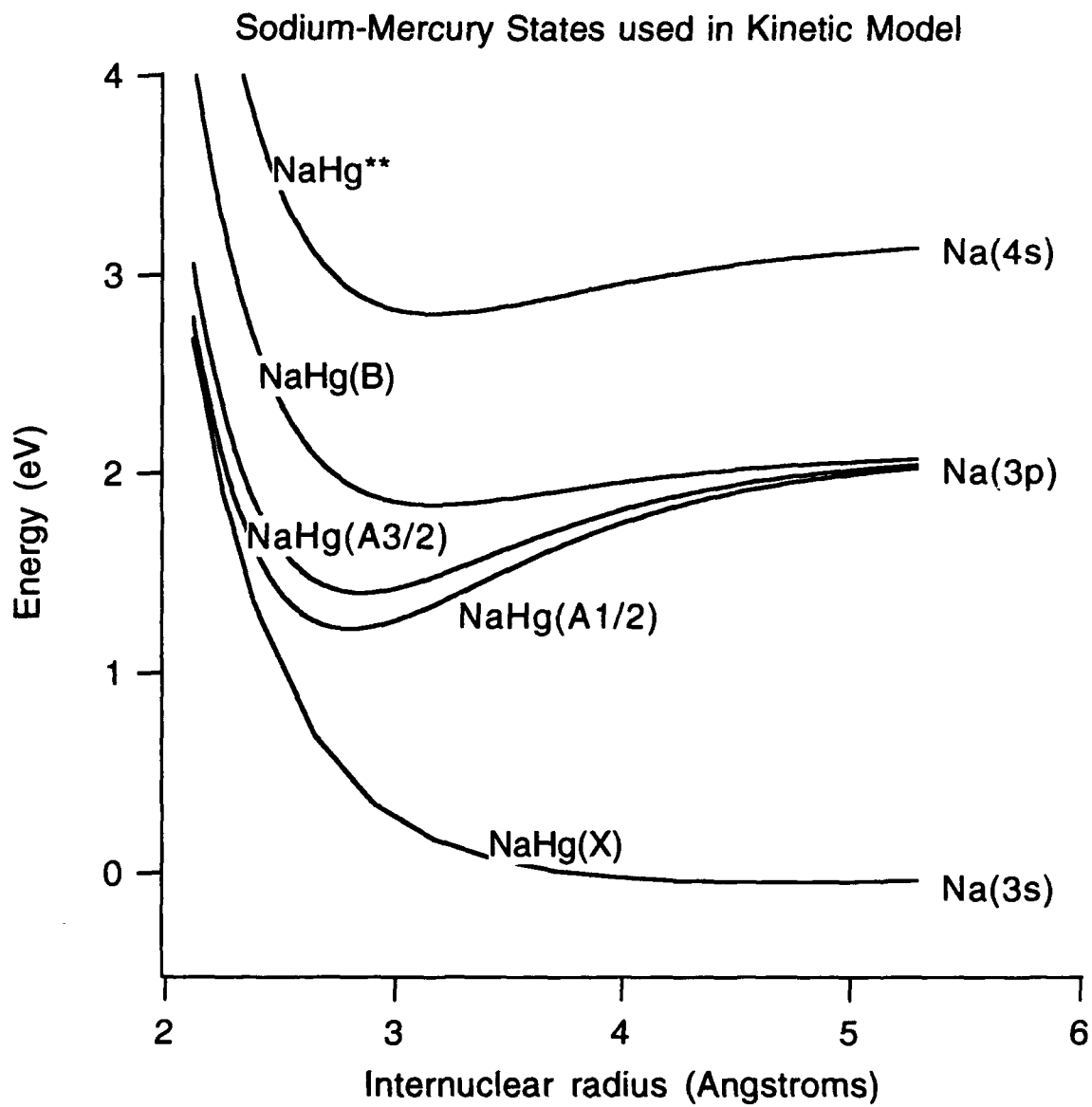


FIG. 4-8 NaHg states involved in kinetic model of NaHg(A-X) laser action.

Table 1. Listing of Processes in Kinetic Model

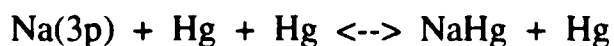
Process #	Process	Rate Constant
	electron excitation	
1	$\text{Na}(3s) + e^- \rightarrow \text{Na}(3p) + e^-$	$f_n(E/N)$
2	$\text{Na}(3p) + e^- \rightarrow \text{Na}(4s) + e^-$	$f_n(E/N)$
	3-body complexing	$(\text{cm}^6 \text{sec}^{-1})$
3	$\text{Na}(3p) + 2\text{Hg} \rightarrow \text{NaHg}(A1/2) + \text{Hg}$	1.5×10^{-31}
4	$\text{Na}(3p) + 2\text{Hg} \rightarrow \text{NaHg}(A3/2) + \text{Hg}$	1.5×10^{-31}
5	$\text{Na}(3p) + 2\text{Hg} \rightarrow \text{NaHg}(B) + \text{Hg}$	1.5×10^{-31}
	collisional dissociation	
6	$\text{NaHg}(A1/2) + \text{Hg} \rightarrow \text{Na}(3p) + 2\text{Hg}$	$f_n(\text{Temp})$
7	$\text{NaHg}(A3/2) + \text{Hg} \rightarrow \text{Na}(3p) + 2\text{Hg}$	$f_n(\text{Temp})$
8	$\text{NaHg}(B) + \text{Hg} \rightarrow \text{Na}(3p) + 2\text{Hg}$	$f_n(\text{Temp})$
	spontaneous emission	sec^{-1}
9	$\text{NaHg}(B) \rightarrow \text{Na} + \text{Hg} + h\nu(650\text{nm})$	6.7×10^7
10	$\text{NaHg}(A1/2) \rightarrow \text{Na} + \text{Hg} + h\nu(1250\text{nm})$	3.9×10^6
11	$\text{NaHg}(A3/2) \rightarrow \text{Na} + \text{Hg} + h\nu(1050\text{nm})$	5.4×10^6
	collisional relaxation	$\text{cm}^3 \text{sec}^{-1}$
12	$\text{NaHg}(A3/2) + \text{Hg} \rightarrow \text{NaHg}(A1/2) + \text{Hg}$	1×10^{-11}
	electron superelastic	$\text{cm}^3 \text{sec}^{-1}$
13	$\text{NaHg}(A3/2) + e^- \rightarrow \text{Na} + \text{Hg} + e^-$	1×10^{-8}
14	$\text{NaHg}(A1/2) + e^- \rightarrow \text{Na} + \text{Hg} + e^-$	1×10^{-8}
	electron mixing	$\text{cm}^3 \text{sec}^{-1}$
15	$\text{NaHg}(A3/2) + e^- \rightarrow \text{NaHg}(A1/2) + e^-$	1×10^{-7}
16	$\text{NaHg}(A1/2) + e^- \rightarrow \text{NaHg}(A3/2) + e^-$	1×10^{-7}
	stimulated emission	$\text{cm}^2 (\text{max})$
17	$\text{NaHg}(A1/2) + h\nu \rightarrow \text{Na} + \text{Hg} + h\nu$	2.7×10^{-17}
18	$\text{NaHg}(A3/2) + h\nu \rightarrow \text{Na} + \text{Hg} + h\nu$	2.4×10^{-17}

Table 1 (contd.)

Process #	Process	Rate Constant
	electron superelastic	
19	$\text{Na}(4s) + e^- \rightarrow \text{Na}(3p) + e^-$	$f_n(E/N)$
20	$\text{Na}(3p) + e^- \rightarrow \text{Na}(3s) + e^-$	$f_n(E/N)$
	3-body complexing	$\text{cm}^6 \text{sec}^{-1}$
21	$\text{Na}(4s) + 2\text{Hg} \rightarrow \text{NaHg}^{**} + \text{Hg}$	1.5×10^{-31}
	spontaneous emission	sec^{-1}
22	$\text{NaHg}^{**} \rightarrow \text{Na} + \text{Hg} + h\nu$	5.4×10^7
	trimer formation	$\text{cm}^6 \text{sec}^{-1}$
23	$\text{NaHg}(A3/2) + 2\text{Hg} \rightarrow \text{NaHg}_2^* + \text{Hg}$	1.5×10^{-31}
24	$\text{NaHg}(A1/2) + 2\text{Hg} \rightarrow \text{NaHg}_2^* + \text{Hg}$	1.5×10^{-31}
25	vibrational relaxation in $\text{NaHg}(A)$ manifold (assumed fast)	
	spontaneous emission	sec^{-1}
26	$\text{NaHg}_2^* \rightarrow \text{Na} + 2\text{Hg} + h\nu$	1×10^6
	collisional deactivation	$\text{cm}^3 \text{sec}^{-1}$
27	$\text{NaHg}(B) + \text{Hg} \rightarrow \text{NaHg}(A3/2) + \text{Hg}$	1×10^{-10}
28	$\text{NaHg}(B) + \text{Hg} \rightarrow \text{NaHg}(A1/2) + \text{Hg}$	1×10^{-10}

4.3.1 3-body complexing and collisional dissociation

The rate of collisional dissociation can be estimated with factor-of-two accuracy by considering the equilibrium between forward and reverse rates in the reaction



where NaHg represents the $\text{NaHg}(A1/2)$, $\text{NaHg}(A3/2)$ or $\text{NaHg}(B)$ states.

The forward rate is $k_{3B}[\text{Hg}]^2$ and the reverse rate is $k_{\text{DISS}}[\text{Hg}]$. In equilibrium,

$$[\text{Na}(3p)]k_{3B}[\text{Hg}]^2 = [\text{NaHg}]k_{\text{DISS}}[\text{Hg}]$$

Independently, from a knowledge of the NaHg state potentials, the equilibrium constant between Na(3p) and NaHg can be calculated using the formalism of York et al. [4], giving a value for

$$K_{\text{EQU}} = [\text{NaHg}] / ([\text{Na}(3\text{p})] \times [\text{Hg}])$$

The required dissociation rate constant is then evaluated from

$$k_{\text{DISS}} = k_{3\text{B}} / K_{\text{EQU}}$$

The rate constant $k_{3\text{B}}$ is assumed to be $1.5 \times 10^{-31} \text{ cm}^6 \text{ sec}^{-1}$ by analogy with the rate for $\text{Hg}(^3\text{P}_1) + 2\text{Hg} \rightarrow \text{Hg}_2 + \text{Hg}$ [8], and varies weakly with temperature. The equilibrium constants are strongly dependent on temperature. Using the molecular potentials discussed in section 4.1 above the equilibrium constants shown in Figure 4-9 were calculated. From these curves we then derived the collisional dissociation rate constants shown in Figure 4-10. For each of the states, at a temperature of 1000K and at 1 Amagat of Hg the dissociation rate is comparable to the radiative lifetime of the state, giving justification for the detailed inclusion of dissociation in the kinetic model.

4.3.2 Spontaneous and stimulated emission.

None of the radiative lifetimes of NaHg A or B states have been measured, so the best indicator is the theory of Windholz et al [1]. These authors calculate oscillator strengths for A-X and B-X transitions as a function of internuclear distance. The radiative rate at internuclear distance R is given in terms of the oscillator strength f as

$$A(R) = \frac{8\pi^2 \nu^2 e^2}{m_e c^3} f_i(R) \frac{g_x}{g_i}$$

where g_x/g_i is the ratio of ground to upper state degeneracies for the transition from upper state i . This ratio is unity for all three states. Whereas the oscillator strength of the B-X transition is calculated to be constant with R, the strength of the A-X transition is projected to decrease as R decreases, losing approximately a factor of five in strength by the time the equilibrium radius is reached. The equilibrium internuclear location contributes most strongly to the maximum in molecular radiation and the stimulated emission cross section at the band center can be found from

$$\sigma = \frac{\lambda^2 A}{8\pi \Delta \nu}$$

where λ is the central wavelength and $\Delta \nu$ is the frequency width (FWHM) of the fluorescence band. Table 2 summarises the data used in the kinetic model.

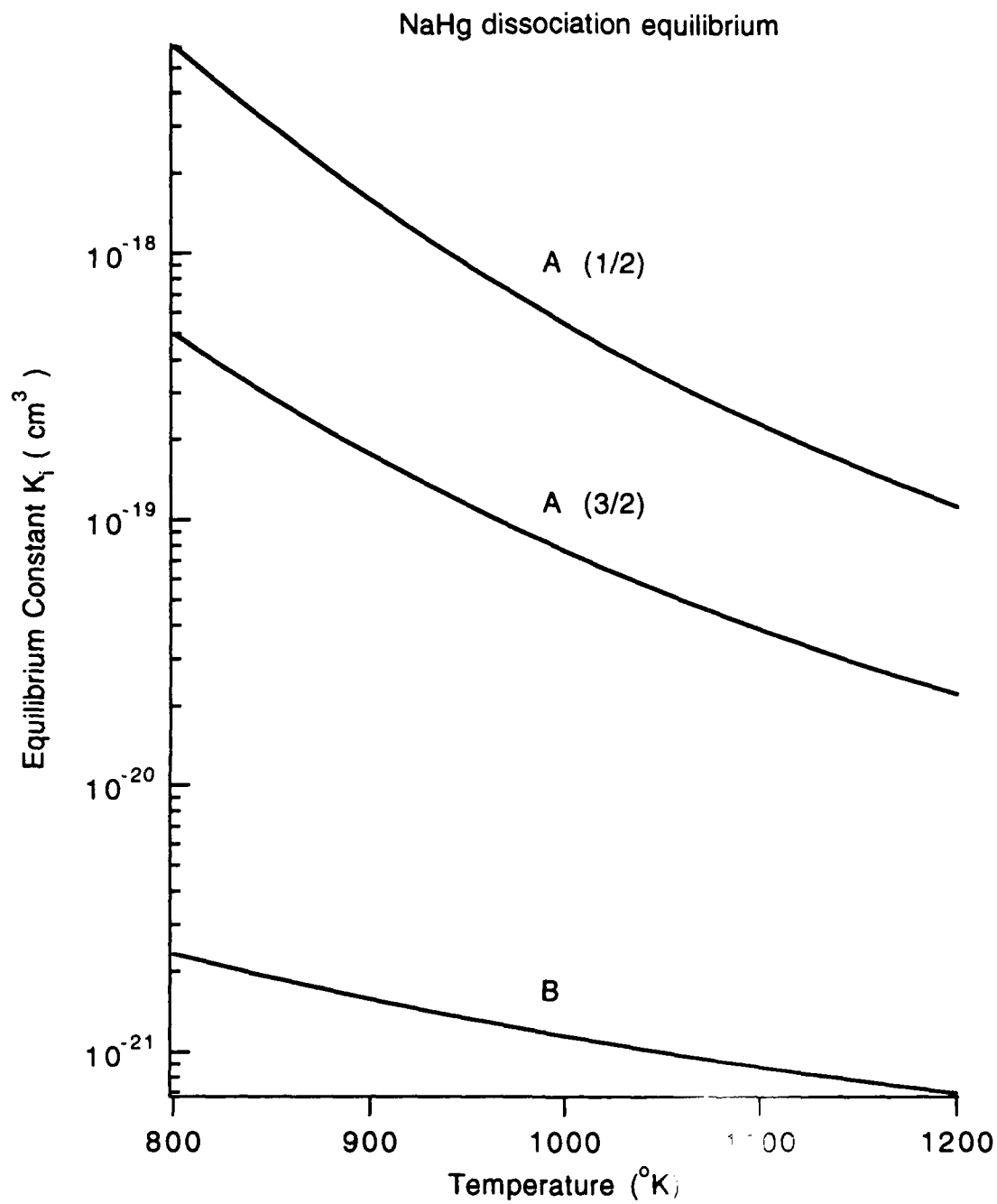


FIG. 4-9 Calculated equilibrium constants for the dissociation of NaHg A and B states.

Collisional dissociation rate constants assuming $k_{3B} = 1.5 \times 10^{-31}$

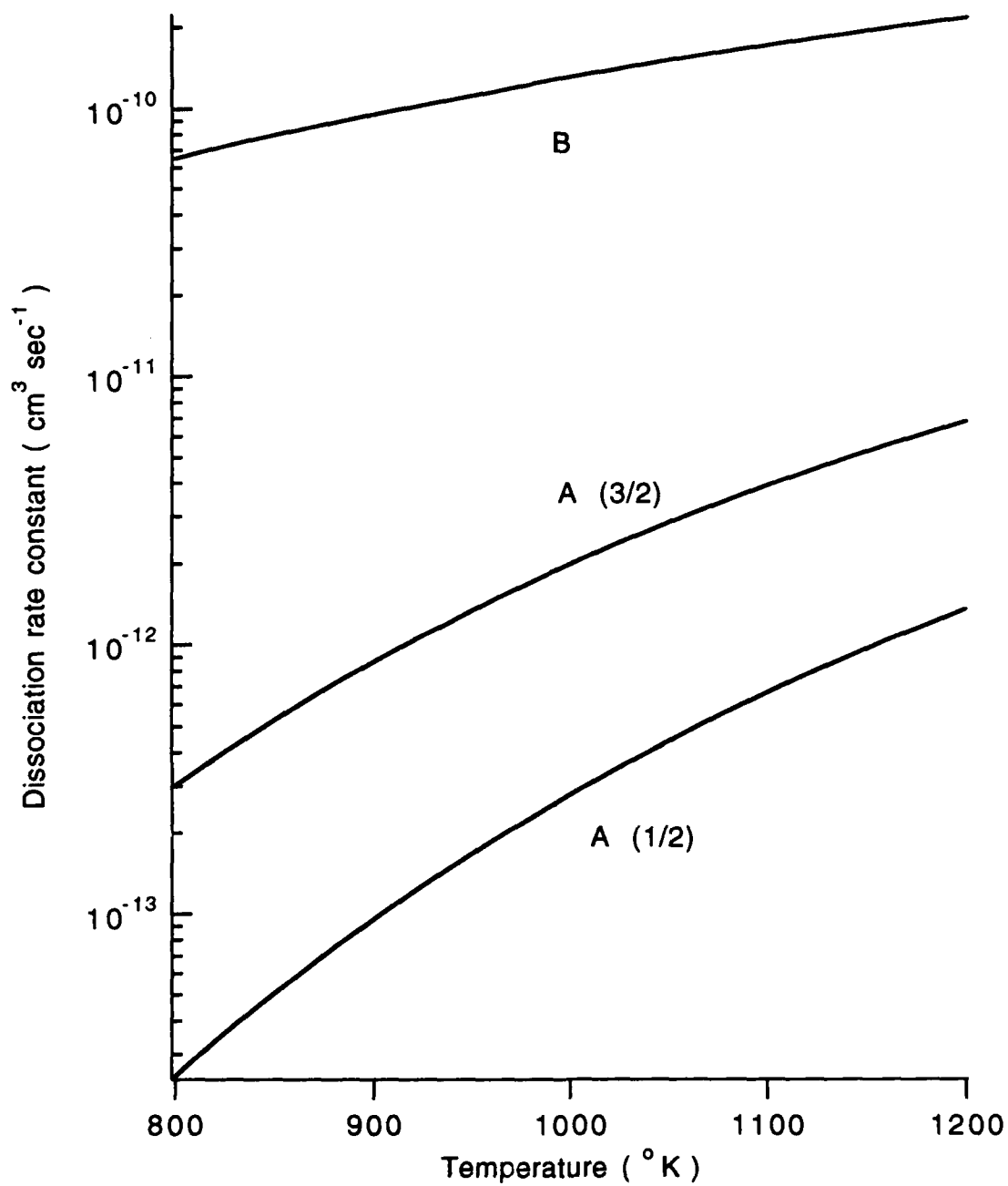


FIG. 4-10 Calculated collisional dissociation rate constants for NaHg states.

Table 2. Spontaneous and Stimulated Emission Rates

Transition	Central λ (nm)	f (R _{EQU})	$\Delta\nu$ (Hz)	A (sec ⁻¹)	τ (nsec)	σ (cm ²)
A1/2 - X	1250	0.09	9.0x10 ¹³	3.9x10 ⁶	256	2.7x10 ⁻¹⁷
A3/2 - X	1050	0.09	1.0x10 ¹⁴	5.4x10 ⁶	184	2.4x10 ⁻¹⁷
B - X	670	0.45	-	6.7x10 ⁷	15	-
C - X	470	0.18	-	5.4x10 ⁷	18	-

4.3.3 Inelastic and superelastic electron rates.

These rates are obtained as output from the Boltzmann calculation for the electron energy distribution function. Some typical values for a mixture with 1%Na and 99% Hg are given in Table 3.

Table 3. Electron Rate Constants (cm³ sec⁻¹)

E / N (Vcm ²)	inelastic		superelastic	
	3s-->3p	3p-->4s	4s-->3p	3p-->3s
2.5x10 ⁻¹⁷	1.6x10 ⁻¹¹	3.6x10 ⁻⁹	3.7x10 ⁻⁷	1.2x10 ⁻⁷
3.75x10 ⁻¹⁷	9.8x10 ⁻¹¹	8.1x10 ⁻⁹	4.2x10 ⁻⁷	1.3x10 ⁻⁷
5x10 ⁻¹⁷	2.4x10 ⁻¹⁰	1.1x10 ⁻⁸	4.4x10 ⁻⁷	1.3x10 ⁻⁷

4.3.4 Gain Projections from Model.

The above processes were assembled into a system of coupled differential equations which was solved numerically using the explicit two-step predictor-corrector method. By setting the electron density to different constant values the discharge specific power could be varied over a wide range. The highest gain was at 1250nm, the central wavelength of the A1/2 - X transition. The gain at this wavelength is shown as a function of specific power in Figure 4-11. The roll-over at high power is due to electron quenching and electron mixing processes. If there

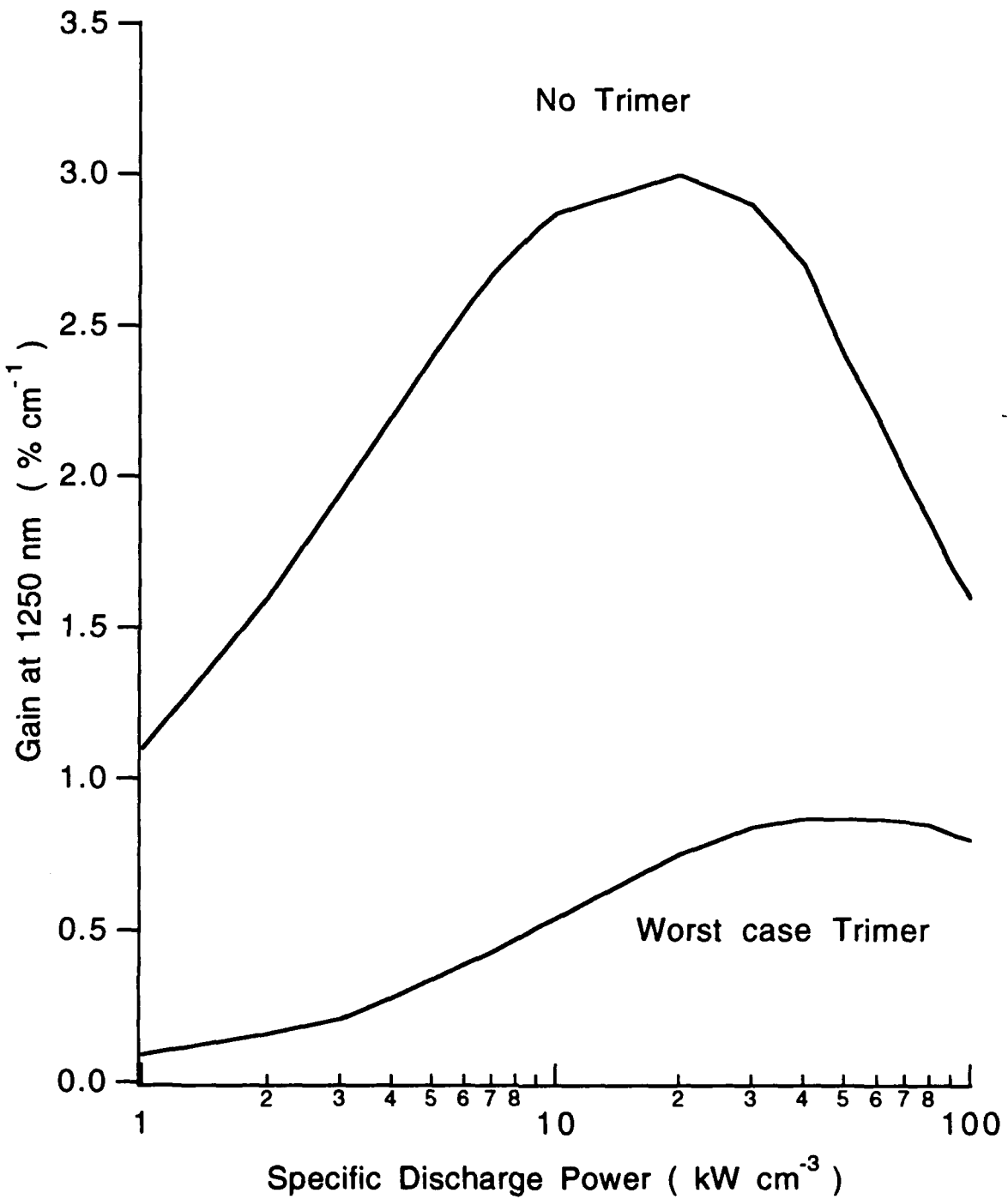


FIG. 4-11 Calculated gain vs specific discharge power for 1%Na, 99%Hg mix at total density $2 \times 10^{19} \text{cm}^{-3}$.

exists a low energy trimer species, the gain is substantially lower. Without the trimer it is maximised for specific powers in the range of 10 to 20 kW cm⁻³, whereas with the trimer it should maximise at 30 - 60 kW cm⁻³.

For example, in an experiment to test for gain which has an active discharge length of 20cm, the maximum gain in a double pass would be 3.3 times, and with a trimer supposed it would be 1.43 times. These numbers indicate that there is a good chance of observing laser oscillation even in a test discharge as short as 20cm, such as the one discussed in the experimental section of this report. In the following section the buildup of oscillations is simulated, in order to estimate the minimum discharge duration needed for oscillation.

4.3.5 Oscillation Projections from Model.

For convenience we follow the two-way photon flux ϕ within a cavity (in units of photons cm⁻² sec⁻¹). For a cavity with active length L_A and total length L_C with a mirror of reflectivity R at one end and a max-reflector at the other, the two-way flux obeys the equation

$$\frac{d\phi}{dt} = \frac{cL_A}{L_C} (\sum \sigma n^*) \phi - \frac{c}{2L_C} (1 - R) \phi$$

in which the sum is taken over the two A states with populations n^* and stimulated emission cross sections σ . This flux equation is integrated with the above kinetic equations using a start intensity corresponding to the spontaneous emission intensity into the oscillating modes.

A typical oscillator simulation is shown in Figure 4-12, in which the output intensity and the NaHg(A1/2) population are plotted as a function of time. The period for buildup of the oscillation is 200nsec in this example, which happens to be for the relatively low pump power of 2kW cm⁻³. The laser output exhibits a "gain-switched spike" at 220nsec, then stabilises at later times, in a manner reminiscent of the CO₂ laser. The NaHg(A1/2) population builds up over a timescale corresponding to its radiative lifetime, which at this relatively low pump power is not much affected by electron quenching. In this example the formation of trimers was not considered. Although requiring higher pump powers, the trimer cases also oscillate in much the same fashion. Either with or without trimer the laser efficiency, defined as the efficiency reached in the steady state, is projected to be 30% at lower pump powers, decreasing as the pump power increases, as shown in Figure 4-13. The efficiency is not decreased in the trimer case because the presence of intense oscillation fluxes intercepts the trimer formation path by reducing the NaHg(A) state population substantially (saturation). The same sort of interception greatly reduces trimer formation in the KrF laser.

Gain Length = 20cm
Reflectivity = 0.9
Discharge 2 kW cm^{-3}
Laser Wavelength 1250nm

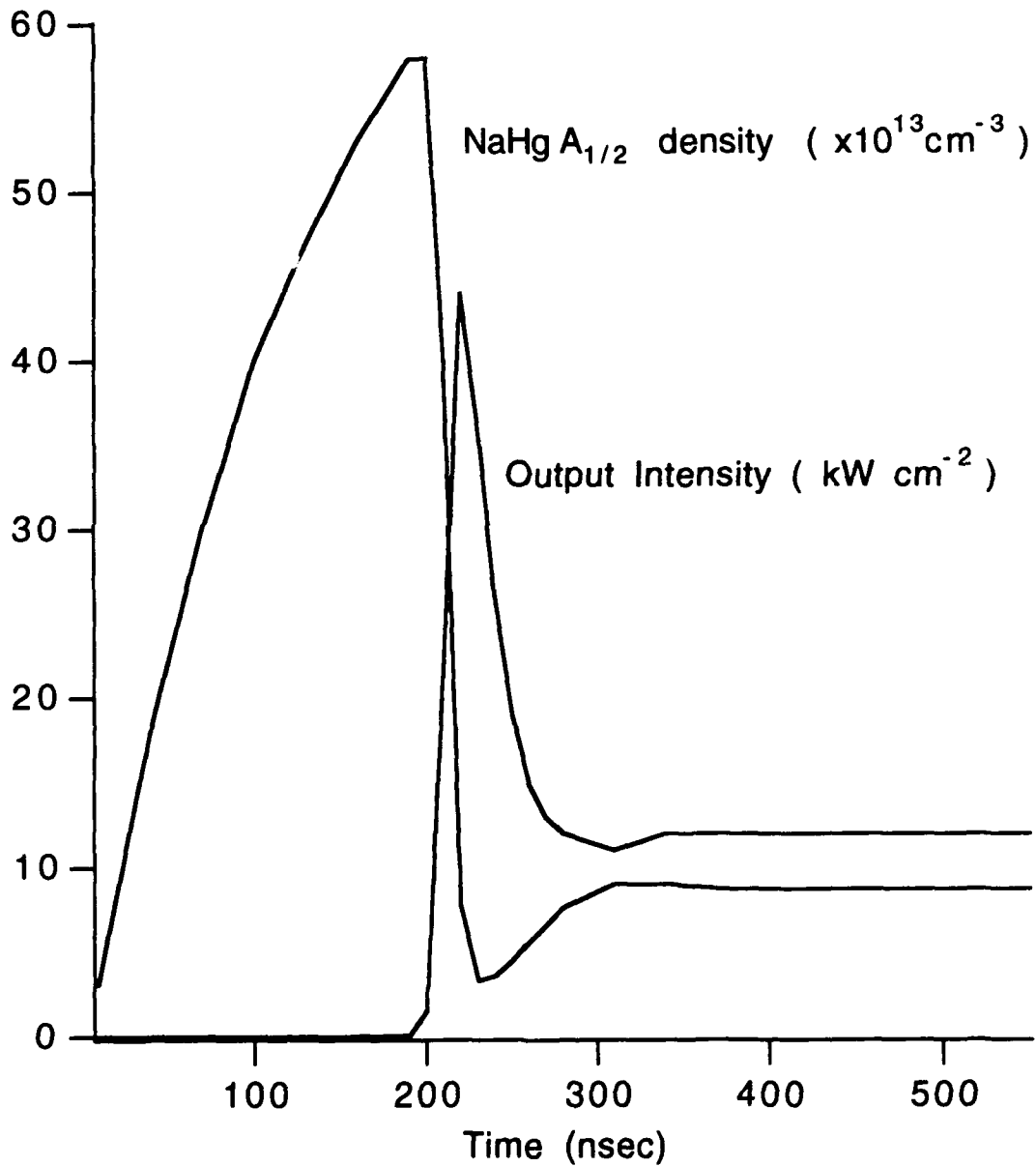


FIG. 4-12 Simulation of NaHg laser performance in 20cm discharge experiment

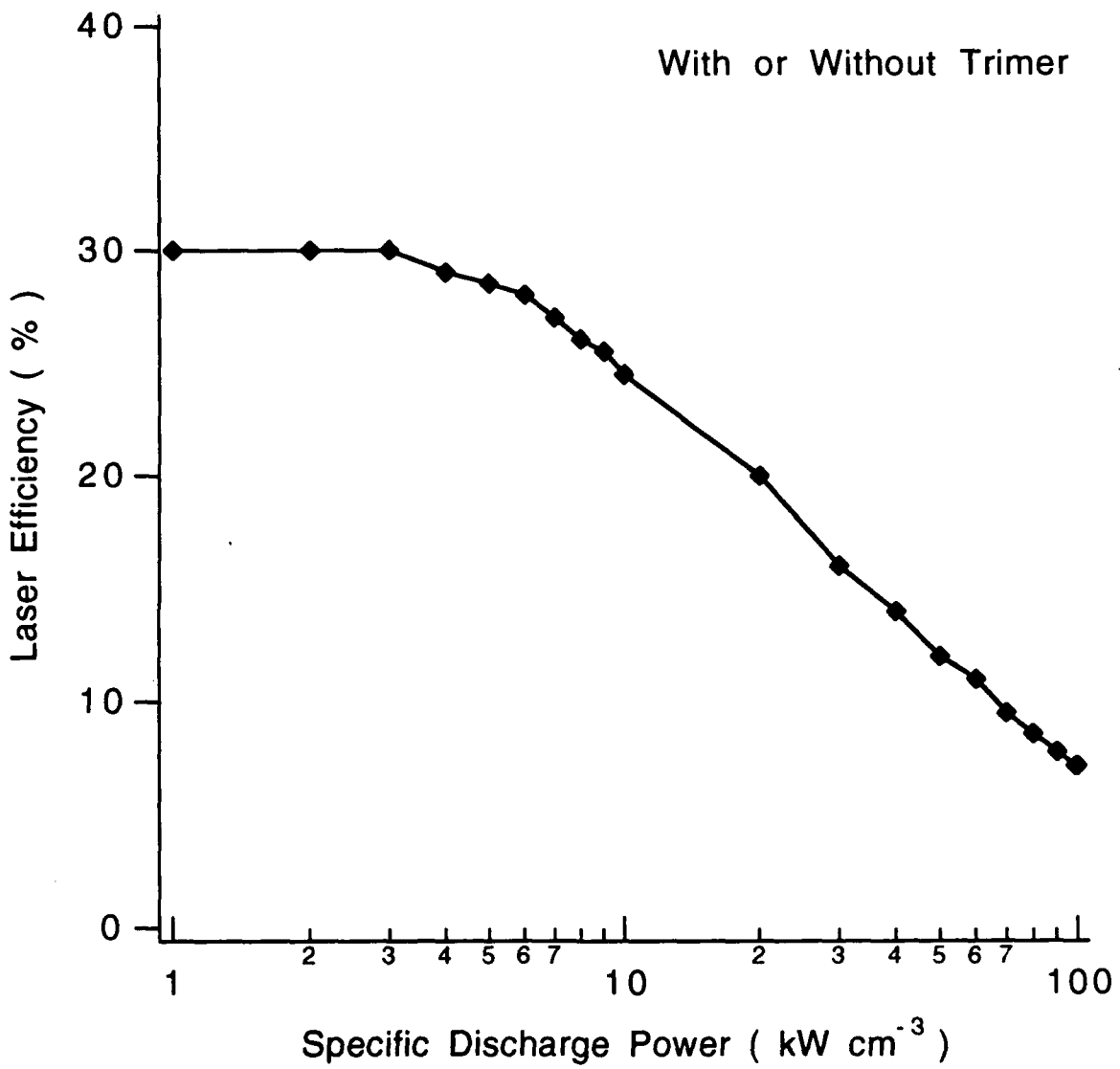


FIG. 4-13 Calculated laser efficiency as a function of specific discharge power.

4.4 Preionisation / Initiation of NaHg Discharge.

The discussion in the previous section has shown that a gain experiment in Na/Hg requires ideally a discharge specific power in the range of 10^4 Wcm^{-3} . At the E/N of $5 \times 10^{-17} \text{ Vcm}^2$ that gives efficient (theoretical) laser action (with $n_{\text{Hg}} = 2 \times 10^{19} \text{ cm}^{-3}$), the electric field is 1000 Vcm^{-1} , so the discharge current density is in the range of 10 A cm^{-2} . The drift velocity in a 1% Na mixture at this E/N is $1.3 \times 10^5 \text{ cm sec}^{-1}$, so an electron density of $5 \times 10^{14} \text{ cm}^{-3}$ is needed to carry this current. In the present section we discuss a method of obtaining this electron density.

Traditionally pre-ionisation is achieved through the use of ultraviolet light, X-rays or an electron beam. The strongest of these is the electron beam method, which has been used to create electron densities of order $1 - 2 \times 10^{14} \text{ cm}^{-3}$ in pure Hg discharges [10], [11]. A much lesser density ($10^9 - 10^{11} \text{ cm}^{-3}$) is achieved using pulsed X-rays, a method which does not appear to have been applied to Hg. The weakest pre-ionisation is via ultraviolet light (usually from sparks adjacent to the discharge region) which photoionises the laser gas. Typically an electron density of $10^7 - 10^{10} \text{ cm}^{-3}$ is achievable by u.v. pre-ionisation in other lasers, most of which contain attaching gases leading to electron removal. There has been work (unpublished) by Hamil on a u.v. pre-ionised Hg discharge (mentioned in ref. 10). The electron beam and X-ray methods require complex apparatus whereas the ultraviolet method is very simple, so the latter method has found by far the most widespread use in pulsed lasers. Ultraviolet pre-ionisation is also the desirable method for the present work, because the laser mixture does not contain attachers, and particularly as a hot experimental cell is used which is difficult to connect to an electron beam apparatus or to an electron beam pumped X-ray source. The source of u.v. radiation can be within the hot cell. In the following discussion it is shown that u.v. pre-ionisation is a very effective process in the case of Na/Hg mixtures.

4.4.1 Avalanche Requirements for NaHg

The initial electron and ion density that exists due to thermal equilibrium in a hot Na/Hg mixture is given by the Saha equation as

$$n_e^2 = \frac{2n_0 g_+}{g_0} \left(\frac{2\pi m_e T_e}{h^2} \right)^{\frac{3}{2}} e^{\left(-\frac{E}{T_e} \right)}$$

where n_0 is the neutral density, g_+ and g_0 are the ion and neutral degeneracies, T_e is the electron temperature and E is the ionisation energy. For example at 600°C and with $n_{\text{Na}} = 2 \times 10^{17} \text{ cm}^{-3}$ the thermal electron density is 10^4 cm^{-3} . The possibility suggests itself of simply applying a high electric field in order to

avalanche these electrons up to the required $5 \times 10^{14} \text{ cm}^{-3}$ density. This, however, is difficult, particularly in small scale discharges, for the following (related) reasons.

1. There is only a limited time available for an avalanche to develop because electrons are being continuously swept out of the discharge (at the drift velocity) by the applied field.
2. This in turn leads to the requirement for a very high applied voltage to achieve a sufficient ionisation rate, but the electrons tend to be swept out faster as the field is increased.

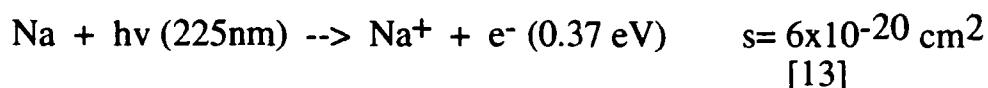
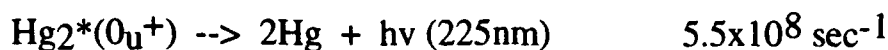
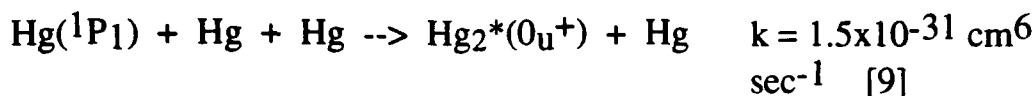
A more quantitative view of α will now be developed. The rate coefficient for the most obvious ionisation process



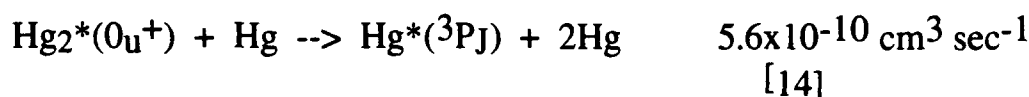
has been calculated in the Boltzmann model of the Na/Hg discharge discussed earlier (Figure 4-6). The calculated ionisation rate constant, given in Fig.4-6, is very small until E/N approaches 10^{-15} Vcm^2 . This behaviour is due to 'screening' of the Na ionisation cross section (threshold 5.138 eV) by the Hg ($^3P_{0,1}$) cross sections (thresholds 4.667eV and 4.886eV). The screening is effective because the Hg number density exceeds the Na density by a factor of 100. The e-folding time constant for the avalanche is given by $t_e = 1/(n_{\text{Na}}k_i)$, where k_i is the ionisation rate constant and n_{Na} is the sodium density. Approximately 18 e-foldings are required between Saha and $10^{11} \text{ electrons cm}^{-3}$, the density at which an energy transfer mechanism of ionisation (discussed below) can take over. The electron drift velocity is given as a function of E/N in Fig. 4-4 . By iteration we find that for an avalanche to go from Saha to 10^{11} cm^{-3} via direct ionisation of Na before electrons can drift by 1 cm requires an E/N of at least $2 \times 10^{-15} \text{ V cm}^2$ (in a 1% Na mixture). This represents a very high applied field. It exceeds the optimum laser excitation field of $5 \times 10^{-17} \text{ Vcm}^2$ by a factor of 40. Typically about 40 kV cm^{-1} would have to be applied to achieve a field-driven avalanche from Saha in the time available and this would pose insulation problems in a laser device.

4.4.2 Ultraviolet Pre-ionisation to $10^{12} \text{ electrons cm}^{-3}$

Clearly the electron density has to be raised above Saha by some technique other than simple overvoltage. It happens that u.v. pre-ionisation is particularly effective in this system owing (a) to the coincidence of the Na ionisation potential with the energy of emission of the $\text{Hg}(2^1P_1)$ state (asymptotic to $\text{Hg}(^1P_1)$) which radiates at 225nm, and (b) the absence of attachers. The u.v. ionisation process depends upon the strong excitation of $\text{Hg}(^1P_1)$ states in a set of intense localised discharges, or sparks. The efficiency of excitation of $\text{Hg}(^1P_1)$ is approximately 20% at $E/N > 2 \times 10^{-15} \text{ Vcm}^2$. Once formed, the following sequence occurs:-



with a competing loss process of collisional pre-dissociation via



It is useful that the 225nm (10nm) fluorescence band is not absorbed significantly by the mercury mixture at densities up to $2 \times 10^{19} \text{ cm}^{-3}$. The binary absorption constant at 225nm is $4 \times 10^{-40} \text{ cm}^5$ [15], implying 0.16 cm^{-1} absorption at this mercury density. The sodium, at lower density, absorbs more weakly in its photoionisation continuum (0.012 cm^{-1} at $2 \times 10^{17} \text{ cm}^{-3}$). The 225nm radiation therefore penetrates many centimeters through the Na/Hg mixtures of interest and produces relatively uniform pre-ionisation. The number density of electrons will now be estimated.

Simple considerations show that the electron density achieved in u.v. pre-ionisation by this route is

$$n_e = \frac{n_{\text{Na}} \sigma_{\text{PI}} E_{\text{arcs}} \eta_{^1\text{P}_1}}{8A \epsilon_i (1 + k_q n_{\text{Hg}} \tau_s)}$$

- where
- n_{Na} = sodium density (cm^{-3})
 - σ_{PI} = photoionisation cross section at 225nm
 - E_{arcs} = total energy (J) in an array of pre-ioniser arcs
 - $\eta(^1\text{P}_1)$ = formation efficiency of $\text{Hg}(^1\text{P}_1)$ in the arcs
 - A = area of spark array (cm^2)
 - ϵ_i = ionisation energy of Na
 - k_q = collisional predissociation rate constant
 - n_{Hg} = mercury density
 - τ_s = spontaneous decay time of $\text{Hg}_2^*(0_{\text{u}}^+)$ state

and a factor of 8 is an approximate geometrical term including radiation only on one side of the spark array, a 50% attenuation in the discharge (screen) electrode and a factor of two reduction due to divergence, the discharge volume being a certain distance from the array.

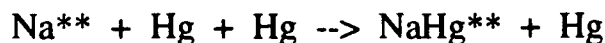
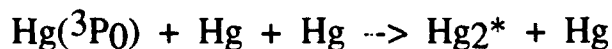
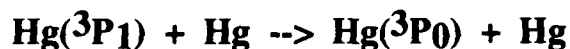
Inserting $n_{\text{Hg}} = 2 \times 10^{19} \text{ cm}^{-3}$, $n_{\text{Na}} = 2 \times 10^{17} \text{ cm}^{-3}$, $\eta(1\text{P}_1) = 0.2$, and the other constants we obtain

$$n_e = \frac{1.7 \times 10^{13} E_{\text{arcs}}}{A}$$

showing that an average spark energy density of only 0.06 Jcm^{-2} will produce $1 \times 10^{12} \text{ cm}^{-3}$ electrons - a density adequate for subsequent multiplication by the energy transfer mechanism discussed below. Provided that this 225nm radiation is delivered in a time short compared to the recombination time there will be no additional electron loss. At the assumed gas temperature of 600°C the dissociative recombination rate constant (presumably fastest via Na_2^+) is $1 \times 10^{-7} \text{ cm}^3 \text{ sec}^{-1}$, so at $n_e = 1 \times 10^{12} \text{ cm}^{-3}$ the recombination time is $20 \mu\text{sec}$.

4.4.3 Final Stage Pre-Ionisation by Energy Transfer.

Beyond 10^{12} cm^{-3} the electron density can be raised to $5 \times 10^{14} \text{ cm}^{-3}$ by a new mechanism which does not require high electric fields. This goes as follows, with the principal forward processes denoted by bold type:-



There is a rapidly increasing rate constant (k_1) for $\text{Hg}(3\text{P}_1)$ formation above $E/N = 5 \times 10^{-17} \text{ Vcm}^2$, reaching $8 \times 10^{-12} \text{ cm}^3 \text{ sec}^{-1}$ at $E/N = 1.5 \times 10^{-16} \text{ Vcm}^2$ (Figure 4-6). Once $\text{Hg}(3\text{P}_1)$ is formed it tends to transfer rapidly into $\text{Hg}(3\text{P}_0)$ which then would complex to Hg_2^* in about 20 nsec at the mercury densities of interest. However, excitation transfer into Na^{**} ($n=6$) occurs with a rate constant as high as $10^{-9} \text{ cm}^3 \text{ sec}^{-1}$ [16], which means that the dominant $\text{Hg}(3\text{P}_0)$ loss route is to Na^{**} for $n_{\text{Na}} > 5 \times 10^{16} \text{ cm}^{-3}$. The last process in the chain, $\text{Na}^{**} \rightarrow \text{Na}^+$, has a rate constant for 1eV electrons of $1 \times 10^{-4} \text{ cm}^3 \text{ sec}^{-1}$ [8], which gives it a rate of $> 10^8 \text{ sec}^{-1}$ for $n_e > 10^{12} \text{ cm}^{-3}$, exceeding possible radiative or collisional decay rates. The whole chain

of events goes at a rate exceeding 10^8 sec^{-1} provided that the electron density exceeds 10^{12} cm^{-3} and the product $k_1 n_{\text{Hg}}$ exceeds 10^8 sec^{-1} . This occurs for $E/N \geq 1.25 \times 10^{-16} \text{ Vcm}^2$. The last 7 e-folds in electron density (from 10^{12} to 10^{15} cm^{-3}) can therefore occur in much less than 10nsec each, at relatively low discharge electric fields (e.g. 3000 V cm^{-1} at $n_{\text{Hg}} = 2 \times 10^{19} \text{ cm}^{-3}$), which are only three times the optimum field for NaHg laser excitation.

Calculations based on the above equations are displayed in Figures 4-14 and 4-15. The calculation is for the 20 cm^2 discharge and includes the 75 nH inductance of the electrode lead in order to evaluate the effect of the $L \text{dI/dT}$ voltage drop caused by a rapidly increasing electron density. Although this effect is substantial, it is only relevant to the last few nanoseconds of the avalanche (Figure 4-14), where it tends to reduce the final electron density reached. Figure 4-15(a) shows the very strong voltage dependence of energy transfer ionisation (due to the $\text{Hg}(^3\text{P}_1)$ excitation rate), and Figure 4-15(b) shows that once adequate voltage is applied, the mechanism should be able to start even at densities as low as $1 \times 10^{11} \text{ cm}^{-3}$.

In conclusion, ultraviolet pre-ionisation has been shown to be an effective route to the achievement of electron densities $> 10^{14} \text{ cm}^{-3}$ in Na/Hg discharges. The pre-ionisation spark energy to achieve 10^{12} cm^{-3} is shown to be modest (about 0.1 J cm^{-2} over the sparkboard) and a rapid new route from 10^{12} to $>10^{14}$ electrons cm^{-3} is available at electric field levels only a factor of three greater than the optimum for NaHg laser excitation.

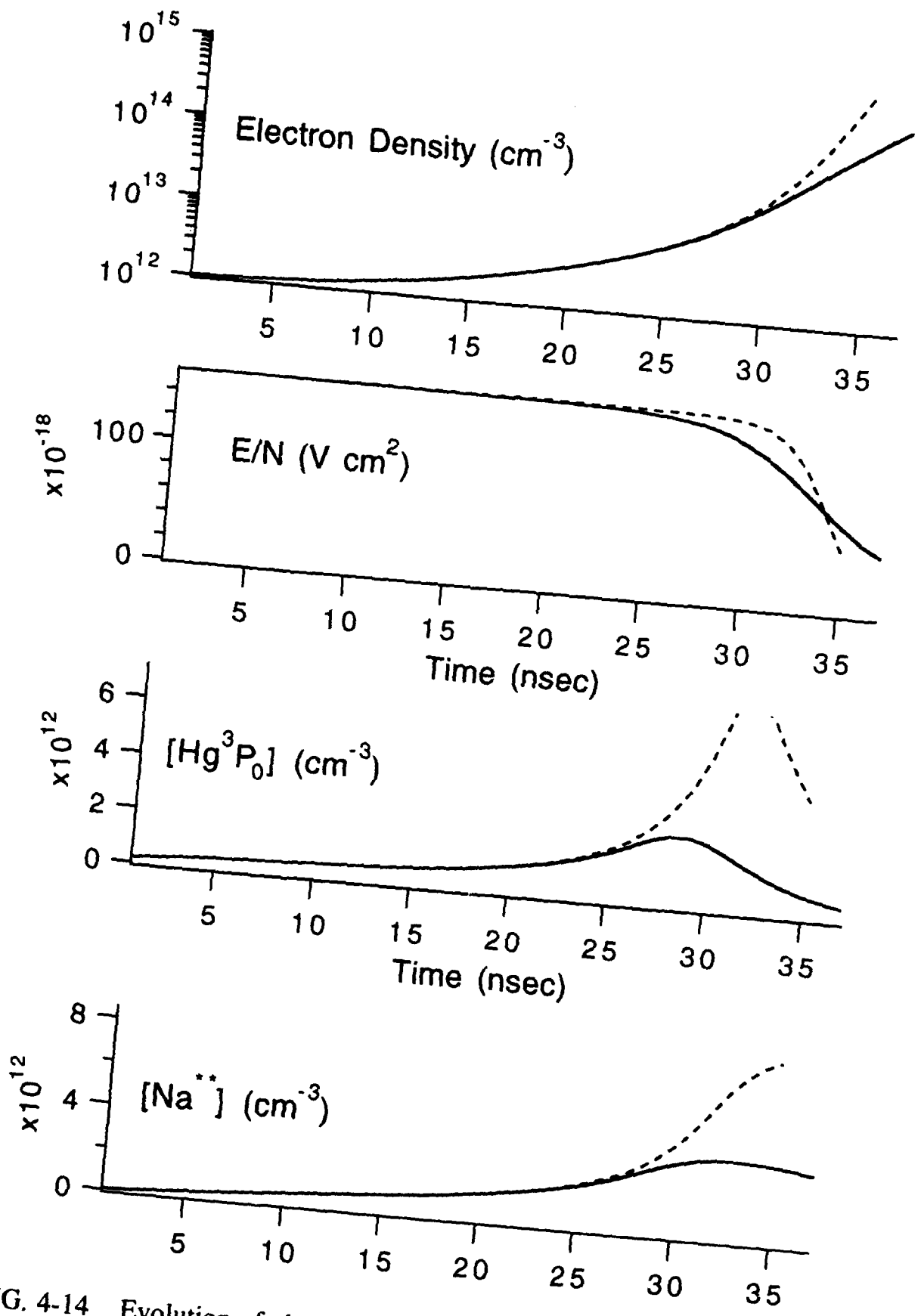


FIG. 4-14 Evolution of electron density, E/N , Hg^3P_0 and Na^{**} for a particular applied field at 75nHlead inductance. Dashed curves are for zero lead inductance.

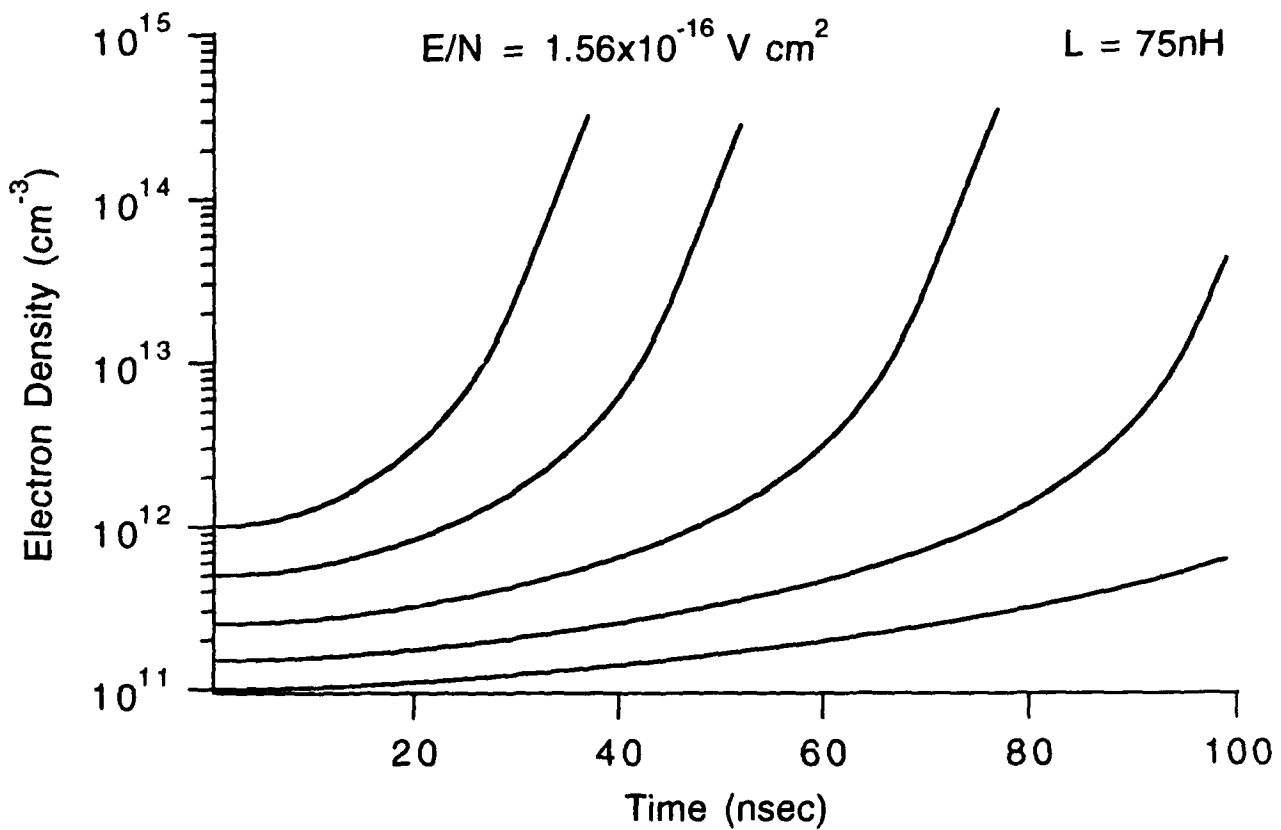
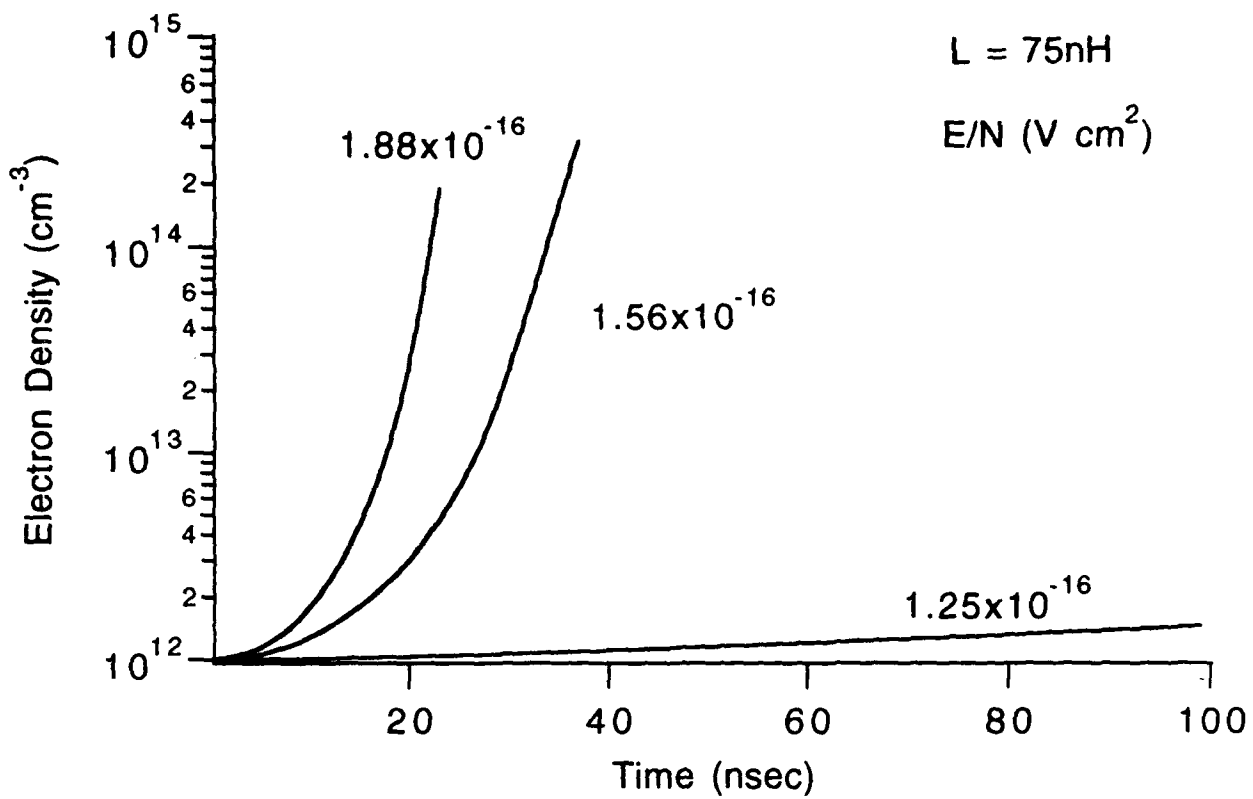


FIG. 4-15 (a) E/N dependence of energy transfer ionisation mechanism.
 (b) Initial density dependence of mechanism.

5.0 Hazard Assessment and Preliminary Hazard List.

The laser gas consists of mercury vapor at approximately 2 atmospheres pressure containing 1% sodium metal vapor. In a 1kW class laser device the mercury content is approximately 150g. Mercury is widely used in industry, science and medicine, but it is a toxic metal, known to accumulate in the body during long exposure. It is planned to avoid any mercury exposure during these tests by means of the following design elements:-

1. The inner cell which contains the metals is of strong stainless steel construction containing substantial ceramic leadthroughs and sapphire windows. It is protected from impact by being located within an outer vacuum vessel, also of steel construction. Any failure of an inner cell seal could only result in a slow release of the metal into the vacuum tight outer cell, where it would condense. The metal mixture that we are considering is widely used in high pressure street lamps, again within a secondary vacuum enclosure.
2. The cell-filling and cell or vacuum chamber opening processes would be carried out under an extraction hood.
3. The rotary motion required within the laser cell to flow the laser medium will be transmitted by magnetic coupling, in order to avoid the otherwise inevitable occurrence of seal leakage.
4. Mercury metal would be recovered and re-cycled using one of several available clean-up kits. The total quantities of mercury used are not great, as the laser medium does not chemically degrade during laser operation, and should be capable of years of sealed-off operation.
5. The sodium hazard is due to the combustible nature of metallic sodium which can spontaneously ignite in contact with water or damp air. The cells which have contained sodium will be opened in an inert atmosphere under an extractor hood, and the sodium mechanically removed and stored under paraffin.
6. Sodium can be separated from mercury by reaction (of the sodium) with water. This reaction would be performed under controlled circumstances in accordance with industry practice.

Preliminary Hazard List.

1. Toxicity: Mercury
2. Combustion: sodium
3. Electrical: Voltages up to 10kV in pulse power circuits.
4. Eye exposure: Depending on the emitted infrared wavelength the laser light may or may not be "eye safe". In any case, there is a laser exposure hazard.

6.0**References**

1. L. Windholz, M. Musso, G. Pichler and B. Hess, J. Chem. Phys. 94, 3366 (1991).
2. L. Huwel, J. Maier and H. Pauly, J. Chem. Phys. 76, 4961 (1982).
3. J. Schlejen, J. P. Woerdman and G. Pichler, J. Mol. Spectr. 128, 1 (1988).
4. G. York and A. Gallagher, JILA Report No. 114, (1974).
5. L. Huwel, J. Maier and H. Pauly, J. Chem. Phys. 74, 5613 (1981).
6. S. D. Rockwood, Phys. Rev. A8, 2348(1973).
7. L. A. Schlie, J. Appl. Phys. 47, 1397 (1976).
8. R. Shuker, A. Gallagher and A. V. Phelps, J. Appl. Phys. 51, 1306 (1980).
9. M. Stock, E. W. Smith, R. E. Drullinger and M. M. Hessel, J. Chem. Phys. 67, 2463 (1977).
10. L. A. Schlie, L. E. Jusinski, R. D. Rathge, D. L. Drummond and R. A. Hamil, J. Appl. Phys. 51, 3137(1980).
11. A. Mandl and M. W. McGeoch, Report 'Metal Vapor Fluorescence Studies' June 1984, Contract DASG60-81-C-0041.
12. R. E. Drullinger, M. M. Hessel and E. W. Smith, J. Chem Phys. 66, 5656 (1977).
13. G. V. Marr and D. M. Creek, Proc. Poy. Soc. A 304, 233 (1968).
14. D. J. Ehrlich anf R. M. Osgood Jr., Chem. Phys. Lett. 61, 150 (1979).
15. M. W. McGeoch, J. Chem. Phys. 72, 140 (1980).
16. J. Maya, Appl. Phys. Lett. 40, 933 (1982).